Inertia and the Critical Scaling of Avalanches in Sheared Disordered Solids

by

K. Michael Salerno Jr.

A dissertation submitted to The Johns Hopkins University in conformity with the requirements for the degree of Doctor of Philosophy.

Baltimore, Maryland

September, 2013

Abstract

This thesis presents results from molecular dynamic (MD) studies of disordered materials undergoing quasi-static shear at zero temperature. Simulations are performed in both two and three dimensions and with a variety of different damping dynamics. During shear, periods of linearly increasing stress and strain alternate with rapid releases of potential energy and stress, termed avalanches. These avalanches have been found in the past to follow power-law statistics. Avalanches in our simulations are observed to exhibit power-law statistics and obey finite-size scaling relations, indicating critical behavior. In contrast with past studies of the nonequilibrium critical depinning transition at the onset of motion, where inertia was observed to destroy critical behavior, we find that inertia qualitatively changes but does not destroy the observed critical behavior. We can characterize three damping regimes, termed overdamped, underdamped and crossover regimes, by measuring scaling and critical exponents in each regime. During each avalanche, potential energy is transformed to atomic motion, with some particles undergoing large displacements. The distribution of particle displacements during avalanche events is quantified, leading to a relation-

ABSTRACT

ship between local plasticity and stress release. Over larger strain intervals particle displacements allow us to quantify an effective strain-dependent diffusion and define a diffusion constant. Avalanche events demonstrate notable spatial correlations over strain intervals large compared with the typical inter-event interval. These correlations are measured using the power-spectrum of measures of the local strain field. The correlations are found to be angle dependent and long range in nature, independent of damping rate.

Thesis advisor: Mark O. Robbins

Acknowledgments

I would like to thank my Physics & Astronomy classmates and IGERT participants for making my education at Johns Hopkins an engaging experience. I would like to thank the Robbins research group members: Ting Ge, Lars Pastewka, Tristan Sharp, Shengfeng Cheng, and Craig Maloney for their discussions regarding physics, science, research and more. Thank you especially to Mark Robbins for his insight, and his example of methodical consideration of physical problems. Thank you to my family, particularly my wife, Cara, whose support and love has helped me along the way.

Contents

List of Tables

List of Figures

Chapter 1

Deformation in Disordered Solids

The study of deformation in disordered solids is of great practical and theoretical interest. A wide variety of materials from many distinct fields can be classified as disordered. Metallic glasses, landslides of rock and soil, colloidal glasses and foams are four very different disordered materials, studied by different classes of engineers or scientists. A better understanding of the response and evolution of these materials when subjected to mechanical deformation could be of great practical use.

Furthermore, the fundamental differences between crystalline and disordered solids make an understanding of deformation, plasticity, and flow in the disordered case theoretically interesting. In crystalline materials the ordered underlying structure leads to a well-defined set of defects that create plastic deformation. On the other hand there is not a fundamental understanding of how plasticity and yielding occur in disordered materials. The loss of rigidity in these materials is still being actively studied.

For example, the jamming and unjamming of granular materials has recently been the subject of a great deal of theoretical and computational study, yielding a non-equilibrium phase transition with a rich phase diagram that is still being explored (Bi et al., 2011).

A comparison between disordered solids and ordered, crystalline solids is helpful on many levels. The lack of understanding of fundamental deformation properties in disordered solids contrasts with knowledge of crystalline materials. The skill with which metals are engineered is a direct consequence of an understanding of their fundamental deformation mechanisms and properties. This fact suggests that much greater control over material properties of, for example, metallic glasses, silicate glasses, granular materials, foams, etc could result from a better theoretical understanding of disordered materials and their deformation.

Many experimental and computational studies have been performed with the aim of understanding the fundamental deformation mechanisms in disordered materials. The work presented in this thesis suggests that the dynamics of constituent particles may have an important role in the growth of plastic deformation from the microscopic scale to larger scales. This idea motivates a close examination of the role of inertia in plastic deformation in disordered solids. The importance of dynamics suggests that while there is much to be learned from computational studies of the singular fundamental instabilities present in disordered materials, knowledge of these instabilities must be set in the context of dynamics. Likewise, experiments, which by definition

always contain dynamics, must be set in a context where the particle dynamics is well known and controlled.

Inertia is not well represented in simplified physical models of deformation and plasticity. Many simplified models of plasticity in solids display the scale-invariant avalanche behavior that is the hallmark of non-equilibrium phase transitions, but nearly all of these models ignore the effects of inertia. It is also not well understood what effect inertia has on basic theoretical models of non-equilibrium phase transitions. The studies presented here could be fundamentally useful if they shed light on how the effects of inertia could be included in theoretical models like the non-equilibrium depinning transition or in mesoscopic models of plastic deformation.

The scale-invariant avalanche behavior studied in the molecular dynamics simulations presented here are a hallmark of non-equilibrium critical phenomena. They are generically seen in a number of overdamped systems that have a non-equilibrium phase transition. The results presented suggest that inertia does not destroy the second-order nature of the transition. Results are specific to the particle model of plastic deformation in disordered solids, but could have interesting implications in a number of different systems. The effects of inertia in critical phenomena are not well understood, and based on results presented, should not be ignored.

1.1 Experimental Studies

Many naturally occurring collections of grains or particles are found in engineering related contexts. For example, sand or beach erosion, soil mechanics and earthquake fault behavior are all influenced by granular packings. Many industrial processes rely on the efficient and safe processing of granular materials, including the processing of products such as pharmaceuticals and grains. Two important aspects of the dynamics of granular media are worth noting. First, grains are generally of macroscopic size, thus thermal fluctuations are not relevant. Second, dissipation in granular media proceeds via frictional forces between particles. Whatever its origins and behavior, this type of dissipation must be Galilean-invariant. Because only relative motion of particles is damped, two adjacent particles moving under the influence of a long-wavelength perturbation feel almost no damping. One particularly dramatic display of this phenomenon is the fundamental modes of the earth, which ring for long periods after large earthquakes. This may have implications at the largest scale and presents a fundamental difference from materials in a viscous medium like colloids or foams, where Galilean-invariance is not respected.

A number of experimental groups study different prototypical granular materials under shear deformation. Losert and coworkers have imaged granular particles in three dimensions in order to examine the network of contacts between particles and its evolution during shear (Slotterback et al., 2012; Herrera et al., 2011). Behringer

and Utter have performed experiments on sheared granular particles and measured affine and non-affine motion (Utter and Behringer, 2004, 2008). These quantities are easily tracked and commonly measured in computational studies. Granular materials commonly respond to mechanical strain with jerky, non-uniform motion. Quantities related to the size of stick-slip events in sheared granular media have been measured by various experimental groups (Hayman et al., 2011; Miller et al., 1996). The measurements made in some of these experiments are similar to the particular measurements made in our simulations, for example, the effective diffusive behavior under shear, and distributions of avalanche events.

Other classes of disordered "solids" commonly used in experiment are foams and emulsions. Viscous dissipation in foams has been measured previously (Cohen-Addad et al., 2004) and (Besson et al., 2008). Experiments suggest that the details of foam dissipation play an important role in bubble rearrangements (Dennin and Knobler, 1997). These materials are often compared with basic computational models of foams.

Another type of disordered solid that experiences viscous dissipation is colloidal glasses. Colloidal particles are between $\sim 0.1 - 1$ micrometer in size, so these systems occupy a length scale between molecular glasses and granular media where particles can be influenced by thermal fluctuations due to the surrounding fluid. With careful preparation these experimental systems can be index matched, so that particle positions can be tracked. Both prototypical deformation events as well as shear rheology have been studied in these types of systems (Chen et al., 2011; Nordstrom et al., 2010).

Other groups have also imaged fundamental defects during shear deformation(Schall et al., 2007).

At the molecular level the most direct comparison with our studies is with metallic glasses, which have been mechanically tested from the macroscopic scale down to nano-size samples. Material scientists and engineers have long been interested in the mechanical properties and deformation of bulk metallic glasses (Wu et al., 2008; Xing et al., 2001). Recently studies have gone to much smaller length scales, finding novel behavior as sample size shrinks (Jang et al., 2011; Jang and Greer, 2010). Nano-pillar size studies hold the promise of meeting the length scale accessible by molecular dynamics simulations. In these systems thermal fluctuations may also be important, particularly if local heating occurs during deformation.

Finally, experiments on the proto-typical granular matter, sand, have hinted at the importance of inertia in such materials. Experiments on cascading sand piles have displayed signs of critical behavior, including a power-law distribution of mass fluctuations which obeyed finite-size scaling (Held et al., 1990). Other researchers studying the relaxation of glass beads to their "angle of repose," found behavior that was not scale-invariant (Jaeger et al., 1989). These researchers found an angular hysteresis, behavior indicative of a first-order phase transition rather than a second-order transition.

1.2 Computational Studies

A variety of different models have been used in computational studies of deformation in materials. These range from models of fibers to fuses to cracks and depinning. A good overview of statistical models and their results is provided in a review article by Alava, Nukala and Zapperi (Alava et al., 2006). These more statistical-physics based models are generally computational expedient and stand in contrast with simulation techniques like molecular dynamics, density functional theory or finite-element models which attempt to correctly capture microscopic details or reflect correct mechanical properties in materials.

One common approach to studying plastic deformation is to use lattice based models with simple site-site interaction rules. These models are closely related to similar models, often called "fuse models." By using lattice-based models and simple updating rules, these models are made to be computationally inexpensive. They also have the advantage that they are often amenable to analytic analysis. For example, fuse models studied by Zapperi et. al. display critical avalanche behavior, and also display a realistic stress-strain relationship (Zapperi et al., 1997). Such models were found long ago to contain many interesting properties and rich phenomena, some of which may be related to plastic deformation or earthquakes (Sornette, 1989). Fuse models are still an area of active research and interest (Shekhawat et al., 2013).

The lattice models described above are all overdamped, and systems that en-

counter an instability evolve only to the first minimum encountered. Other computational models have added inertia-like effects to basic models. For example the canonical sandpile model of Bak, Tang and Wiesenfeld has been studied with inertial effects by Prado and Olami (Prado and Olami, 1992). More closely related to inertia in granular materials and disordered solids are studies of the Burridge-Knoppof model including inertial effects. The basic model describes a set of linear elements interacting via springs (Burridge and Knopoff, 1967). When inertial effects are added, no tuning of disorder is necessary to produce a power-law distribution of slip sizes (Carlson and Langer, 1989). These models disregard the details of the particle-level physical interactions, considering only discrete scalar values on a lattice. Other models, built up from microscopic interactions do better in this area.

A number of groups have looked at the mechanical response of foams using computational models. These computational models mimic experiments by applying viscous dissipative forces to the constituent bubbles. Ono and coworkers have examined bubble velocity fluctuations in one particular model of a sheared foam (Ono et al., 2003). A study of the same model foam examined the statistics of bubble rearrangements, finding a power-law distribution of rearrangements (Tewari et al., 1999). Other researchers have also studied similar models and found consistent avalanche distribution results (Durian, 1997).

Atomistic simulations fill an important role in the simulation of materials. They do not require any coarse-graining or ad-hoc assumptions about material properties,

other than about the basic particle scale interactions. As a result, they provide the microscopic detail that continuum or lattice based models lack. Molecular dynamics simulations are an excellent tool for studying microscopic deformation mechanisms and have been used extensively for this purpose. Quasi-static, energy-minimization (athermal) simulations are a particularly clean way to measure the fundamental properties of mechanical instabilities in sheared disordered materials (Maloney and Lemaître, 2004b; Maloney, 2006; Tanguy et al., 2006; Demkowicz and Argon, 2004; Karmakar et al., 2010). To date, there has not been a full characterization of the fundamental properties of such instabilities. Such a characterization could be a breakthrough in the study of disordered materials as it could allow mesoscopic models based on these elements to be formulated.

Unfortunately, the atomistic detail of molecular dynamics comes with the computational cost of integrating Newton's equations of motion for each particle. Energy minimization is potentially less computationally demanding, yet even these types of simulations require calculating forces between each particle and its neighbors. This cost limits simulations to somewhat small numbers (millions) of particles, and relatively short times (nano-seconds). In the case of mechanical deformation this also limits the systems studied to relatively high strain rates.

Molecular dynamics simulations have also examined different aspects of how mechanical instabilities trigger one another and build up into what are termed avalanches. These avalanches can lead to interesting behavior in particle displacements and plas-

tic deformation over large strain intervals. Bailey and coworkers have measured avalanche sizes in sheared quasi-static three-dimensional simulations (Bailey et al., 2007). Lemaître and Caroli have measured particle displacements and diffusion in two-dimensional solids both at finite strain rate (Lemaître and Caroli, 2009) and in quasi-static simulations (Lemaître and Caroli, 2007). Maloney and Robbins also looked at particle displacements and diffusion in two dimensions at finite strain rate (Maloney and Robbins, 2008) in a study related to their finding of angle-dependent power-law correlations in plasticity over large strain intervals (Maloney and Robbins, 2009). Both Lerner and Procaccia, as well as Maloney and Lemaître, have measured avalanche size distributions in two-dimensional, quasi-static simulations (Lerner and Procaccia, 2009; Maloney and Lemaître, 2004b).

Recently, molecular dynamics simulations have also become a common tool in the study of macroscopic granular materials, based on models of contact interactions for macroscopic particles (Brilliantov et al., 1996; Silbert et al., 2001; Zhang and Makse, 2005). This has led to the use of molecular dynamics in the analysis of a wide variety of problems, both of a fundamental and of an applied nature (Silbert et al., 2009; Zhang and Makse, 2005). This type of simulation benefits greatly from straightforward and direct comparison with analogous experiments (Clark et al., 2012; Kondic et al., 2012).

Some attempts have been made to include important microscopic details in meso-scale or lattice-based models of plasticity in disordered solids. In the case of ordered

materials, discrete dislocation dynamics would be an example of this approach, using dislocations as the representative plastic element in a crystal. Simulations of this type allow for large crystal volumes to be simulated with realistic plastic flow behavior (Miguel et al., 2001). Similar attempts have been made at modeling important spatial correlations between areas of plastic deformation in disordered materials with promising results (Talamali et al., 2011). In these types of models information from atomistic simulations may be important in building up mesoscopic models for the defects.

1.3 Analytical Models

Most theoretical work related to deformation and plasticity in disordered materials is based on a model of an elastic manifold driven through a random medium by an applied force. These models focus on the non-equilibrium "depinning" transition, between the stationary or "pinned" phase and the non-stationary or "depinned" phase as force increases. The velocity of the elastic manifold can be interpreted as the order parameter, with zero velocity in the pinned phase and non-zero velocity in the depinned.

The depinning transition has been found to apply to many different physical systems, indicating that, at least in this sense, the transition is universal. Systems such as fluid invasion in porous media, magnetic domain wall motion in soft ferromagnetic

materials, charge-density wave motion and flux-line lattices in superconductors all exhibit the phenomenology typical of the depinning transition (Fisher, 1985; Martys et al., 1991a; Dahmen and Sethna, 1996; Myers and Sethna, 1993).

Renormalization group analysis of the model charge-density wave system pinned by impurities and driven by an electric field was originally carried out by Narayan and Fisher for the case of overdamped equations of motion (Narayan and Fisher, 1992). Critical exponents found in these studies agree with simulations of cellular automata (Myers and Sethna, 1993).

Models with stress overshoots like those caused by inertia have been studied by various researchers, notably Schwarz and Fisher, however relatively less attention has been given to such models (Schwarz and Fisher, 2003, 2001; Marchetti, 2005). One common approach is to add rules that lower barriers to motion when an avalanche starts (Prado and Olami, 1992; Maimon and Schwarz, 2004; Dahmen et al., 2009; Friedman et al., 2012; Dahmen et al., 2011). This fits the intuitive picture that inertia can carry a system over successive potential energy barriers, but inertia is highly directional, and decreases the chance of passing over barriers that are not in the direction of the momentum. These models have predicted a tricritical point where the transition changes from second to first-order. Furthermore, there are subtle aspects the inclusion of inertia in lattice models which seem to indicate that hysteresis may occur in an infinite system, even while the transition is second order (Maimon and Schwarz, 2004; Marchetti, 2005). Theoretical analyses have so far not provided

a clear picture of what the effect of inertia is in the depinning transition.

Models of driven manifolds and depinning have been applied to the study of dislocation motion in crystalline solids. Mean-field models of depinning have successfully described some quantitative aspects of deformation in single-crystal samples (Friedman et al., 2012). Experiments on single-crystal mechanical testing are difficult, but many researchers have measured data consistent with mean-field theoretical and simulation models (Zaiser, 2006).

The success of mean-field models in describing crystalline plasticity may be due in large part to a detailed understanding of the microscopic deformation mechanisms, *ie* dislocations, and their interaction and motion. Such a detailed understanding of fundamental deformation units in disordered materials does not exist, though much theoretical and computational work has been performed on the subject.

Theories of fundamental deformation mechanisms in disordered solids have long been an area of active research. Models specific to metallic glasses were developed in the 1970s following the introduction of the material in the 1960s (Argon, 1979; Spaepen, 1977). These original theories involved simple free-volume arguments and results from earlier studies of plastic deformation within an elastic medium (Eshelby, 1957). Progressive updates have improved upon the basic theories by refining free-volume arguments.

Most recently, shear-transformation zones have been proposed as fundamental defects that allow statistical theories for flow to be developed (Falk and Langer,

1998). Progress is being made not only in probing and defining these "generalized dislocations" of disordered solids, but also in working out their statistical properties, evolution and behavior in non-equilibrium systems (Manning et al., 2009; Falk et al., 2004; Langer, 2012). Unfortunately the idea of a mesoscopic computational analysis akin to discrete dislocation dynamics based on fundamental rules for defect creation, interaction, motion and annihilation does not exist. Some computational approaches incorporating important features of shear transformation zones are currently used, reproducing fundamental physical phenomena (Talamali et al., 2011).

1.4 Outline of Thesis

The introduction in the previous paragraphs has given some context for the type of numerical study undertaken in this thesis. The different experimental systems mentioned in the introduction are relevant to various aspects of the simulation methodology. Where appropriate, particular experimental materials, computational methods or results will be compared with the results found in our studies.

Chapter 2 describes the basic parameters of the molecular dynamics studies in this work, including the sample preparation and mechanical deformation protocol. The size, geometries, and composition of the systems studied in both two and three dimensions are enumerated. Particle interactions including pairwise interactions and dissipative potentials are described. In particular, the dissipative potentials employed

and the strength of that dissipation form the basis of our studies on the role of inertia in the critical behavior observed in strained disordered solids. The deformation protocol used is described in detail. This includes a description of how the quasi-static limit is reached. Finally, a simulation protocol for straining systems at finite rate is outlined. A comparison of finite strain rate and quasi-static simulations is presented.

Chapter 3 presents a study of the critical and scaling exponents related to the avalanche event distributions in the systems studied. Interesting behavior in the fluctuations of shear stress and potential energy motivate a closer examination of these quantities. Rate distributions of stress and energy fluctuations are formed and some scaling properties of these distributions are derived. Finite-size scaling analysis is applied to the distributions of stress and energy drops associated with each avalanche, based on exponent relations derived in the chapter. The scaling analysis provides a picture of the influence of inertia on the critical behavior in the solid. The chapter also describes the dependence of the steady state shear stress on system size and damping regime. Finite-size scaling is also used to determine scaling exponents for the distribution of stress values, which can be related to scaling exponents for other critical properties.

Chapter 4 describes the fundamental differences between two types of dissipation, one which respects Galilean-invariance and one which does not. Avalanche distributions and their scaling exponents are used to compare and contrast the universal behavior observed for different damping mechanisms.

Chapter 5 gives a definition of plastic deformation in molecular dynamics simulations. The plastic deformation during individual avalanche events is described, and the effects of damping on plastic deformation are shown. Chapter 5 also shows some of the large-strain behavior of the solid materials simulated. Over many avalanches, patterns emerge in certain measures of the deformation. Interesting correlations in the plastic strain in similar simulations have been found in the past. These results are extended through measurements of plastic strain correlations to a variety of system parameters. Previous results for effective particle diffusion are also confirmed, with an estimate of the system-size dependent diffusion constant in two dimensions. These results are contrasted with results from three dimensions where the effective particle diffusion is independent of system size.

Finally, some conclusions are presented in Chapter 6 with a discussion of questions raised by the results presented and possible directions for future research.

Chapter 2

Simulation Methods

This work builds on the basic simulation methods and protocols used in previous studies exploring the fundamental mechanisms of plastic deformation (Maloney and Lemaître, 2004a; Tanguy et al., 2006; Falk and Langer, 1998). The particle interactions and sample preparation have also been used previously in the study of disordered solids (Falk and Langer, 1998; Maloney and Lemaître, 2006). Of more interest and distinction are the dynamics implemented in our simulations. Together, the deformation protocol and dissipation mechanisms govern the unique features of how the system dynamically evolves with applied strain. The details of these features lead directly to the rich phenomena observed in the simulations that make up the main results of this work.

Previous simulations modeling sheared disordered solids have generally fit into two distinct frameworks: studies where deformation is carried out in the quasi-static

limit and studies at finite strain rate. Studies at finite strain rate require a form of dissipative damping, with different viscous (Ono et al., 2003) and Galilean-invariant (Maloney and Robbins, 2009; Lemaître and Caroli, 2009) dissipative models used previously. Historically, quasi-static deformation has been implemented as small finite strain perturbations to a system coupled with energy-minimization dynamics (Lemaître and Maloney, 2006; Maloney and Lemaître, 2006; Lemaître and Caroli, 2007; Tanguy et al., 2006).

The simulations presented in this work examine deformation in both the quasi-static limit and at finite rate. Some simulations are performed in the overdamped or energy-minimization limit. We also examine the under-appreciated, but crucial role that inertia can have in the evolution of sheared disordered solids. This work also compares both viscous and Galilean-invariant dissipative potentials, the details of which are outlined below.

2.1 Particle Interactions

This thesis presents results from molecular dynamics (MD) simulations of deformed disordered solids in two and three dimensions. In all cases, the system studied is a binary glass. The two species of particles A and B both have mass m, but have different diameters to prevent crystallization. The particles interact via a smoothed Lennard-Jones (LJ) potential, which depends only on the magnitude r of the vector

r between two particles and their species. This potential keeps the standard LJ form at small distances:

$$U(\mathbf{r}) = 4u[(a_{ij}/r)^{12} - (a_{ij}/r)^{6}] + u_c \quad , \quad r < 1.2a_{ij}, \tag{2.1}$$

where u is the interaction energy, u_c is an energy offset, and a_{ij} is the interaction length between particles of type I and J. For the interaction form given, the binding energy is of order $u/2$. The $A - A$ particle interaction length is taken as the fundamental unit of length $a \equiv a_{AA}$. The $B - B$ particle interaction length $a_{BB} = 3/5a$, while the mixed interaction length $a_{AB} = a_{BA} = 4/5a$. Outside the LJ region the potential has a polynomial form

$$U(\mathbf{r}) = C_1(r - r_{ij}^{(c)}) + \frac{C_2}{2}(r - r_{ij}^{(c)})^2 + \frac{C_3}{3}(r - r_{ij}^{(c)})^3 + \frac{C_4}{4}(r - r_{ij}^{(c)})^4 \quad , \quad 1.2a_{ij} < r < 1.5a_{ij}, \tag{2.2}$$

with coefficients C_i chosen so that the energy, force and the derivative of the force match the LJ form at the inner cutoff radius, $1.2a_{ij}$, and go to zero at an outer cutoff radius, $r_{ij}^{(c)} = 1.5a_{ij}$. The strength of the interaction, particle radius, and mass set the fundamental unit of time, $t_0 = \sqrt{ma^2/u}$. Simulations were performed with the LAMMPS MD simulation code, using a velocity-Verlet integration algorithm with an integration timestep $\Delta t = t_0/200$ (Plimpton, 1995).

Other interaction potentials including a harmonic potential and a truncated LJ potential have also been implemented in order to check whether particle interactions play a key role in the dynamics of the system. These have been used in a limited

number of simulations without varying other parameters, but results produced are consistent with the results presented for the truncated LJ potential.

2.2 System Preparation

Two-dimensional systems are initialized by placing particles at random in a square periodic simulation cell with the ratio of the number of particles of species A and B: $N_A/N_B = (1+\sqrt{5})/4$. Next, the system is heated well above the glass transition temperature and then quenched to zero temperature at constant pressure. The pressure is chosen to be slightly compressive, $\sim 0.1u/a^2$, in order to avoid voids. Following this procedure the system density is $\rho = 1.38a^{-2}$ and the square simulation box has period L. We consider five box sizes with $L = 55a, 109a, 219a, 437a$ and $875a$. These sizes correspond to $N \approx 10^3$ to 10^6 particles.

A similar equilibration protocol is followed for three dimensions. After equilibration the density is $\rho = 1.7a^{-3}$ and the simulation is a cube with period L. Sizes are $L = 20a, 40a, 81a$, and $162a$, corresponding to $N \approx 10^3$ to 10^7 particles.

2.3 Deformation Protocol

After the quench process the samples are strained by affinely displacing each particle to match the change of the periodic boundaries. The deformation applied to the simulation box in two dimensions is a pure shear strain at a true strain rate

$\dot{\epsilon} = \dot{\epsilon}_{xx} = -\dot{\epsilon}_{yy}$. In three dimensions the system volume is conserved by applying an axisymmetric compressive true strain rate $\dot{\epsilon}$ in two dimensions (x and y) and an extensional strain rate $2\dot{\epsilon}$ in the third dimension (z).

Simulations in two dimensions using a simple shear deformation geometry were also performed. These simulations tested whether simulation geometry influenced the behavior observed. These simple shear simulations tested a variety of other parameters and in all cases produced avalanche dynamics and system evolution consistent with the pure-shear geometry. We concluded that deformation geometry plays little role in the avalanche phenomena observed in our simulations. This leaves open the possibility that other deformations such as an applied compression or tension may lead to different behavior, *e.g.* if void formation becomes important. Similarly, we cannot rule out that some results regarding the angular dependence of correlations in chapter 5 may be geometry dependent.

2.4 Dissipation

Our aim is to study the athermal limit, which requires constantly removing kinetic energy from the simulation. In our basic and most well-studied system a viscous drag force is applied to damp particle motion. The drag force has the form $\vec{F}_{drag} = -\Gamma_v m\vec{v}$ where $\vec{v}$ is the peculiar velocity. The peculiar velocity is that due only to particle interactions, with displacement due to the affine deformation subtracted. The

dissipation rate Γ_v plays a central role in our simulations by controlling the relative importance of the inertial term in the particle equations of motion. As Γ_v decreases, the dynamics changes from overdamped to underdamped (inertial) dynamics.

For comparison we also simulate systems with particle motion damped by a Galilean-invariant damping mechanism. The force applied to particle i for this damping mechanism is

$$-\Gamma_G m \sum_j (\vec{v}_i - \vec{v}_j) f(r) \tag{2.3}$$

where the radial function $f(r)$ follows the cutoff distances set by the smoothed LJ potential.

$$\begin{aligned} f(r) &= 1 - \tfrac{r^2-(6a_{ij}/5)^2}{(3a_{ij}/2)^2-(6a_{ij}/5)^2} \qquad && r > 1.2a_{ij} \\ f(r) &= 1 && r < 1.2a_{ij} \\ f(r) &= 0 && r > 1.5a_{ij} \end{aligned} \tag{2.4}$$

The Galilean-invariant damping mechanism has been used in previous studies of sheared disordered solids at finite strain rate (Maloney and Robbins, 2008; Lemaître and Caroli, 2009). This dissipative potential has the interesting feature that the effective damping time for a perturbation on length scale ξ is $\tau_{eff} \propto \xi^2$. This means that long wavelength modes can persist for long times, even when motion at the particle scale is overdamped. This damping mechanism serves two purposes. First, it provides a check that the behavior observed is not an artifact of the viscous damping mechanism. Second, macroscopic systems of interest like granular packings should have no particle dissipation in the $\xi \to \infty$ limit.

Below we will make the distinction between Γ_v and Γ_G when comparing the two damping mechanisms directly in Chapter 4. Results in Chapters 3 and 5 all are from simulations using viscous dissipation. The symbol Γ with no subscript will be used to refer to phenomena which are independent of particular dissipation mechanism; but rather reflect behavior that is independent of the damping form. For example in the limit of large Γ we expect results from both dissipation mechanisms to be equivalent to energy minimization dynamics.

2.5 Response

Generically, a strained disordered solid will load elastically for some strain interval and then plastically deform, decreasing the stress in the system and releasing stored elastic energy as kinetic energy. These sudden bursts of particle motion are termed avalanches. In the quasi-static limit the series of elastic loading segments and plastic deforming avalanche events should be independent of strain rate and depend only on the total strain interval. One way to realize this limit is to deform the system at a very low strain rate. In this case the kinetic energy from one avalanche has been dissipated long before the system has been strained enough to nucleate the next avalanche event. Since the rate must be set low enough to prevent overlap of the closest events, this is not computationally feasible for all system sizes and damping rates. Instead, we implement a protocol where the system is strained at a finite strain

rate, which is then reduced to zero when an avalanche is detected.

A representative strain-avalanche-strain interval, shown in Fig. 2.1, illustrates how the system evolves with this quasi-static avalanche detection scheme. When the system is deformed, the non-affine response due to heterogeneity in the solid produces a small background kinetic energy density, KE_{back}. This kinetic energy is nearly constant during elastic loading at constant strain rate (solid lines). When an avalanche starts, there is a sharp rise in kinetic energy. The strain rate is reduced to zero when the kinetic energy exceeds KE_{back} by roughly two orders of magnitude. The straining of the solid resumes when the kinetic energy has fallen below KE_{back} by at least two orders of magnitude. We have checked that the strain rate chosen is low enough that the results are not sensitive to these thresholds.

The stress response of the system illustrated in Fig. 2.1b is typical, showing linear behavior during the strain interval, followed by a rapid drop during an avalanche event. During avalanches with low particle damping the stress often overshoots the steady-state value which is used to quantify the size of avalanches. Such drops can complicate the identification of slip events by local minima in the stress-strain curve in analyzing simulations or experiments at constant strain rate.

Even after eliminating the connection between strain rate and avalanche duration, there is still the problem of the very long duration of large avalanches at very low damping rates. As the damping coefficient Γ becomes small and events become large, the peak kinetic energy in the system approaches $10^{-3}u$ per unit area (volume). At

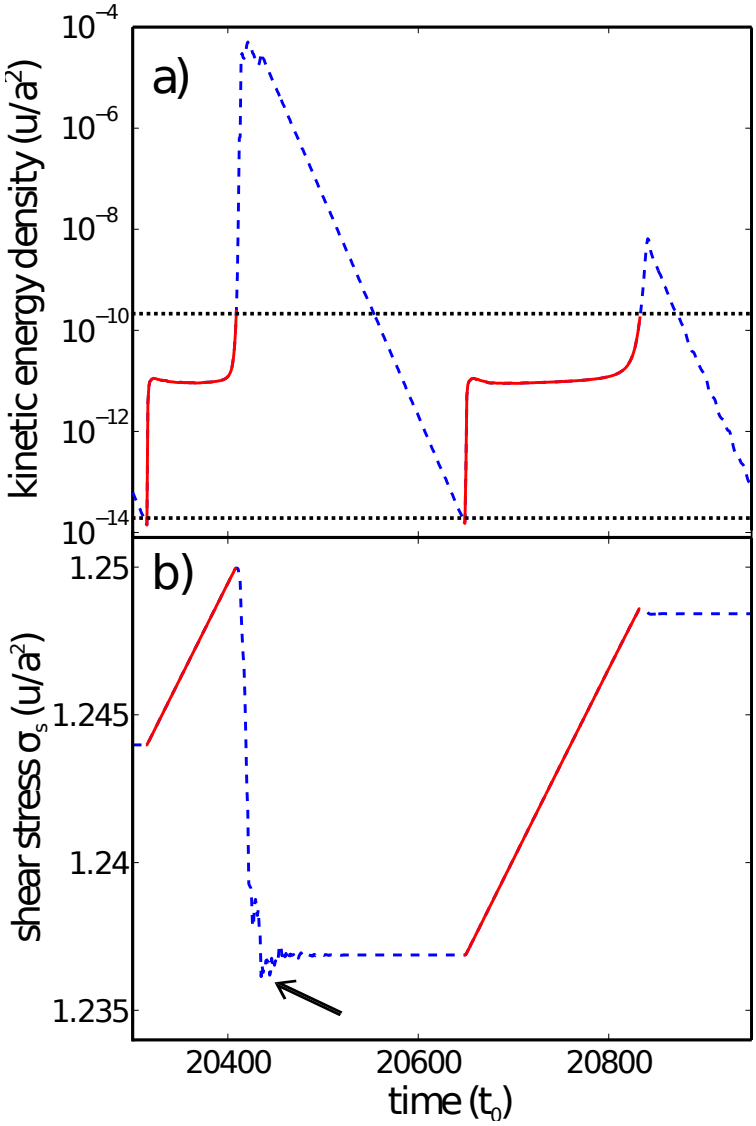

Figure 2.1: a) An event sequence showing the kinetic energy thresholds (dotted horizontal lines) used to reach the quasi-static limit. Here an $L = 219a$ system is strained at a rate of $\dot{\epsilon} = 10^{-6}t_0^{-1}$ during the solid (red) segments and the low, constant kinetic energy reflects non-affine displacements due to heterogeneity. Avalanches cause a sharp spike in kinetic energy that decays more rapidly as Γ increases. The strain rate is set to zero (dashed blue segments) after the upper threshold is exceeded and returned to $10^{-6}t_0^{-1}$ when a lower threshold is passed. b) The stress-strain curve rises linearly during elastic loading (solid red) and drops rapidly as the avalanche begins (dashed blue). There is often an overshoot (arrow) where the stress drops below the steady-state value.

our prescribed strain rates there is then a factor of $KE_{max}/KE_{back} \approx 10^8$ between the maximum kinetic energy and the kinetic energy during straining. This energy must be removed by the viscous drag force and one can estimate that for the smallest damping rates we simulate, $\Gamma_v t_0 = 10^{-3}$, the decay of the kinetic energy will take a time of about $\log(KE_{max}/KE_{back})/\Gamma_v \approx 20,000 t_0$. This is not only computationally expensive, but unnecessary. Even for our largest system sizes the time for sound waves to propagate across the system, $t_{prop} = L/c \approx 250 t_0$, is much smaller. Systems seldom show signs of further instability, such as kinetic energy spikes or stress drops, after about $2 - 3 t_{prop}$.

In order to expedite draining the system of kinetic energy when $\Gamma_v t_0 = 10^{-3}$, we quench the kinetic energy rapidly once a threshold has been reached. Our criterion is that when the kinetic energy in the system has fallen to about 10^{-3} times the peak kinetic energy the avalanche is effectively over and no other instabilities will be activated. For the viscous damping force discussed above, this is equivalent to a time criterion since the decay of the kinetic energy in the system is exponential. For comparison, the time for this decrease in kinetic energy is still roughly ten times larger than the timescale for sound to propagate across the largest simulation cell ($L = 875a$). It is also much larger than the time for the stress to reach its steady-state value (Fig. 2.1), indicating an event is over.

In order to verify that the quench procedure does not affect system evolution, we compared it to simulations with constant damping. For a subset of avalanches

simulated with both the "quench" protocol and fixed damping rate, the total energy dissipated differed by less than $10^{-9}u$. This is orders of magnitude smaller than the smallest avalanches recorded, which have energy $E \approx 10^{-5}u$. We conclude that the quench protocol produces a system in the same local potential energy minimum as the unquenched simulation.

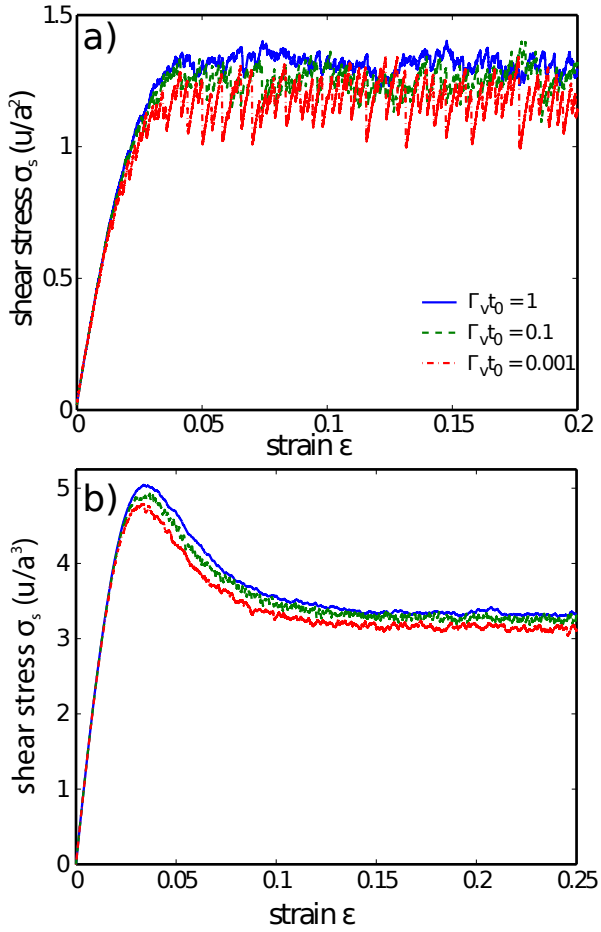

Figure 2.2: Typical stress-strain curves in a) two and b) three dimensions for three different damping rates, $\Gamma_v t_0 = 1$ (solid blue), $\Gamma_v t_0 = 0.1$ (dashed green), $\Gamma_v t_0 = 0.001$ (dashed-dot red). Systems reach steady state at about 7% strain in two dimensions and about 14% strain in three dimensions.

Generically, the elastic energy density stored in a system by a differential strain $d\epsilon$ is $du_{strain} = \sigma_{ij} d\epsilon_{ij}$, where σ_{ij} is the stress tensor, and summation over repeated indices is implied. Because the 2D strain geometry is pure shear, this can be simplified by defining $\epsilon \equiv \epsilon_{xx} = -\epsilon_{yy}$ and $\sigma_s \equiv \sigma_{xx} - \sigma_{yy}$. The stored elastic energy density is then

$$du_{strain} = \sigma_s d\epsilon. \tag{2.5}$$

The elastic strain energy in three dimensions has the same form if one defines $\sigma_s \equiv \sigma_{xx} + \sigma_{yy} - 2\sigma_{zz}$ and $\epsilon \equiv \epsilon_{xx} = \epsilon_{yy} = -1/2\epsilon_{zz}$.

Typical stress-strain loading curves are shown in Fig. 2.2. In two dimensions the systems reach steady-state after roughly 5% strain for all damping rates. In three dimensions the steady state regime occurs at larger strain, between 10 - 15%. There is a small drift in the hydrostatic pressure up to strains of order 20%, but quantities of interest like the shear stress and avalanche statistics become stationary and do not evolve with strain. Only avalanches at strains greater than 7% in two dimensions and 14% in three dimensions are included below.

2.6 Finite Strain Rate

While the quasi-static deformation protocol has the advantage that all the details of each avalanche can be recorded, there are some drawbacks that make a finite strain rate deformation protocol advantageous. One of the main drawbacks of the

quasi-static protocol is the computational cost. As described earlier, it can often be many simulation timesteps before the activity associated with an avalanche event is completely damped out. Simulating at a finite strain rate implies that multiple independent events will occur during overlapping time intervals. If the strain rate causes these events to influence one another then the evolution of the system at finite rate will be significantly different from the same system in the quasi-static limit.

Other groups have previously studied the crossover from finite strain rate to the quasi-static limit. Caroli and Lemaître found that at strain rate $\dot{\epsilon} \sim 1/L^2$ two-dimensional systems cross over from displaying highly correlated avalanche-induced plasticity to plasticity that occurs as uncorrelated noise (Lemaître and Caroli, 2009). While scaling results presented below suggest that the relationship between the quasi-static definition and strain rate is more complicated, this relationship is a reasonable rough estimate.

Figure 2.3 shows the dependence of the mean steady-state shear stress as well as the RMS fluctuations as a function of strain rate for $L = 875a$. For three representative damping rates $\Gamma_v t_0 = 1$, $\Gamma_v t_0 = 0.1$, and $\Gamma_v t_0 = 0.001$ values of the mean and standard deviation of the steady-state stress are near their quasi-static values for $\dot{\epsilon} \leq 10^{-6} t_0^{-1}$.

Finite-strain rate simulations have been used to expedite the collection of statistics for some quantities presented in chapters 3 and 5. Quantities such as the particle displacement and shear stress have values that are correlated over large strain intervals.

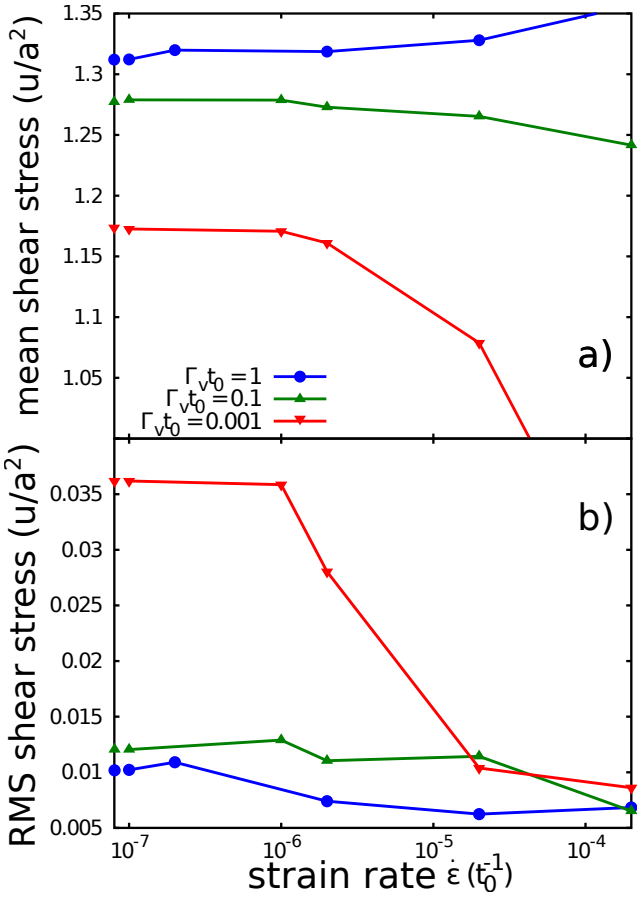

Figure 2.3: Steady-state a) mean shear stress and b) RMS shear stress as a function of strain rate for the largest two-dimensional system simulated, $L = 875a$. Quasi-static values are marked along the y-axis. Values reach their quasi-static limit below $\dot{\epsilon} = 10^{-6} t_0^{-1}$. The curves reflect the approach to the quasi-static limit at finite strain rate.

Implementing a finite strain rate is the most effective way to generate statistically independent strain intervals.

For both the quasi-static and finite strain-rate results below we strain all systems at $\dot{\epsilon} \leq 2\text{x}10^{-6}$. For quantities related to the $L = 875a$ systems we use systems strained at $\dot{\epsilon} \leq 10^{-6}$ and $\dot{\epsilon} \leq 2\text{x}10^{-7}$. These rates all fulfill the bound given by Caroli and Lemaitre, and we have checked that quantities of interest agree between the finite strain-rate protocol and quasi-static protocol.

Chapter 3

Avalanche Distributions

Shear stress and potential energy fluctuations display behavior that changes dramatically with the strength of the applied dissipative damping. In this chapter we demonstrate the importance of inertia or damping in governing the size and rate of avalanche fluctuations in the quasi-static simulations described in Chapter 2. These results can be compared with previous experiments, simulations and analytic predictions of avalanche size distributions in comparable systems as described below.

We compare avalanche rate distributions for both stress and potential energy drops, and explore the close relationship between shear stress and potential energy. Finite-size scaling is performed using the avalanche rate distribution, and critical scaling exponents are found. Critical scaling exponents can be related to the distribution of steady-state shear-stress values. A finite-size scaling of the distribution of these values is also performed.

One common method for studying plastic deformation is to use a lattice based model with simple site interaction rules. These models are computationally and analytically tractable, but have the limitation that positions and stress changes are discrete. Most studies consider scalar quantities and are in the overdamped, mean-field limit where correlations in deformation are ignored. In these limits, mean-field models produce a power-law avalanche distribution of avalanche sizes with a universal power-law exponent $\tau = 3/2$ (Alava et al., 2006; Dahmen et al., 2011). One lattice model that takes the tensor nature of stress and strain into account displays long-range correlations in deformation that match atomistic models and produces avalanches that follow a power-law distribution with exponent $\tau = 1.25$ (Talamali et al., 2011). Models with different rules for site evolution, like long-term damage to sites, also find different power-law exponents for avalanche statistics (Zapperi et al., 1997).

The avalanches of plastic deformation that occur in strained disordered solids have been studied in a number of experiments. Many research groups have performed studies of experimental systems such as granular packings, colloidal glasses, foams and metallic glasses under deformation (Schall et al., 2007; Utter and Behringer, 2004, 2008; Hayman et al., 2011; Miller et al., 1996; Wu et al., 2008; Xing et al., 2001; Jang et al., 2011; Jang and Greer, 2010). While experimental systems provide a real-world test of physical behavior there are limitations inherent in experiments. In addition to the limitations to adjustable parameters, it is often difficult to apply finite-size scaling analysis due to limited sizes. In studies on granular media Hayman

has reported cumulative avalanche probability distributions with power-law behavior, but with exponents much larger than mean field predictions, with τ between 3.5 and 6.0 (Hayman et al., 2011). Sun and coworkers have reported results from deformation of bulk metallic glasses, finding avalanche distribution exponents τ between 1.3 and 1.5 (Sun et al., 2010, 2012).

Some research groups have used similar molecular dynamics simulation methods to ours, recording avalanche distributions for different geometries and system parameters. Lerner and Procaccia have simulated two-dimensional systems under quasi-static shear in the overdamped limit and measured an exponential avalanche cutoff that scaled with system size (Lerner and Procaccia, 2009). Though a power-law distribution of avalanches was not measured, the system size scaling is consistent with critical behavior. Maloney and Lemaître studied energy-minimization dynamics for quasi-static shear in two dimensions, finding avalanches that followed a power-law distribution, with a slope τ between 0.5 and 0.7, and a cutoff that grew with system size (Maloney and Lemaître, 2004b). Bailey and coworkers recorded avalanche size distributions in three-dimensional simulations, also measuring a system-size dependent cutoff (Bailey et al., 2004). Related computational models of bubbles in the overdamped limit have also found a power-law distribution of rearrangements with exponent $\tau = 0.7$ (Tewari et al., 1999; Durian, 1997). The computational studies described above have all been of size 100 particles across or less. These sizes are relatively small in comparison with the discrete particle size, restricting the range of

scale-free critical behavior.

Both the above experimental and computational studies suggest that in sheared amorphous solids avalanche activity can span a wide range of sizes with interesting size dependence. Quantities similar to those measured in our simulations have been measured previously both experimentally and in simulation. Due to inherent experimental limitations finite-size scaling is not usually applied in an experimental setting. Previous workers have found results different from the current findings, but with similar phenomenology. In some experiments and simulations, particularly (Sun et al., 2010) and (Carlson et al., 1991), results quite similar to ours have been found, though the fundamental role of inertia was not identified or fully explored.

3.1 Stress and Energy Fluctuations

This section illustrates some of the dramatic effects that inertia has on the mean of and fluctuations in the shear stress and potential energy density in steady-state, quasi-static shear. One limiting case is the overdamped (large Γ) regime, where the potential energy decreases monotonically to the next minimum during each avalanche. In the opposite, underdamped limit, there is negligible damping during plastic rearrangement, and inertia can carry a system over successive small energy barriers. We present typical results from these limiting regimes with damping rates $\Gamma_v t_0 = 1$, and $\Gamma_v t_0 = 0.001$, respectively. There is also a critical intermediate damping rate of

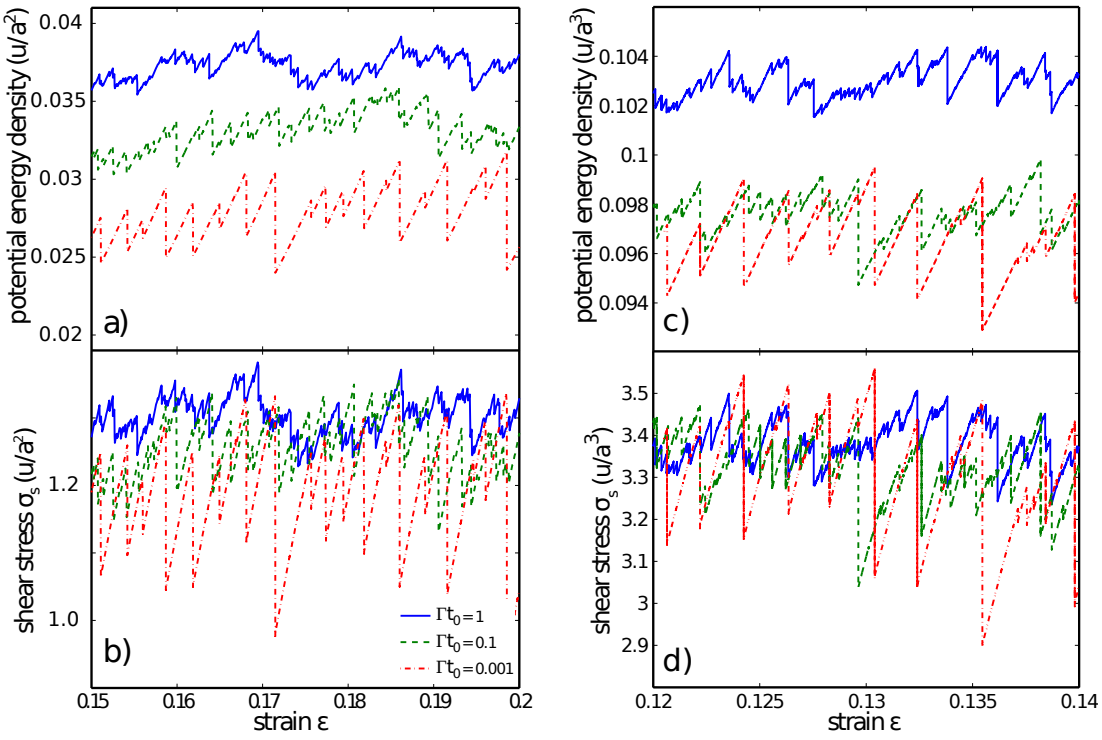

Figure 3.1: The a) potential energy density and b) stress for a two-dimensional system and c) potential energy density and d) stress for a three-dimensional system during a representative strain increment. In both two and three dimensions the systems began at the same zero-strain particle configuration but evolved with different, representative damping rates: $\Gamma_v t_0 = 1$ (solid blue), $\Gamma_v t_0 = 0.1$ (dashed green) and $\Gamma_v t_0 = 0.001$ (dash-dot red) The mean values and the size and rate of fluctuations in energy and stress vary significantly with damping rate. System sizes are $L = 219a$ in two dimensions and $L = 40a$ in three dimensions.

$\Gamma_v t_0 = 0.1$ that separates these regimes. We find that this crossover damping rate is the same in two and three dimensions within our uncertainty.

Figure 3.1 illustrates how damping affects the potential energy density and stress. Note that in two dimensions systems with different damping rates sample completely different potential energies with almost no overlap. Differences of approximately 30% in the mean value of the potential energy density persist in our largest system sizes. There is a smaller but significant difference of about 10% in the mean stress. In three dimensions the mean potential energy in the overdamped and underdamped limits varies by about 8% and the stress by 6%. As the damping decreases, inertia is able to carry the system over barriers in the potential energy landscape to progressively lower minima. In addition to reducing the mean potential energy, inertia leads to larger avalanches. The increase in the size of energy and stress drops is evident in Fig. 3.1 and related to changes in scaling exponents discussed below.

As illustrated in Fig. 3.1, the evolution of the stress and potential energy density is characterized by linear rises, where elastic energy is stored, and sudden drops during avalanches. Each avalanche can be characterized by the potential energy density drop $\Delta\mathcal{U}$ and stress drop $\Delta\sigma_s$. In what follows we want to compare avalanches of the same absolute size in systems of different linear dimension L. We define absolute measures of stress and energy drop as

$$E \equiv L^d \Delta\mathcal{U}, \quad S \equiv \frac{\langle\sigma_s\rangle L^d}{4\mu}\Delta\sigma_s \qquad . \tag{3.1}$$

The shear modulus μ and the steady-state shear stress $\langle\sigma_s\rangle$ are introduced so that

both S and E have units of energy. We have found that both μ and $\langle\sigma_s\rangle$ are nearly independent of system size and relatively insensitive to damping rate. Fixed values of $\langle\sigma_s\rangle$ and μ are used for all L and Γ.

The quantities S and E can be related by a sum rule, which follows from energy conservation. Each avalanche event, i, is accompanied by a potential energy density drop $\Delta\mathcal{U}^{(i)}$ and shear stress drop $\Delta\sigma^{(i)}$. This dissipated energy must be balanced by the work done on the system during segments where the system loads elastically. For a strain segment $\Delta\epsilon^{(j)}$ the work done on the system is $\sigma_s\Delta\epsilon^{(j)}L^d$.

The assumption that there is a well defined steady-state mean potential energy density allows us to equate the sum of the energy drops with the total work done

$$\sum_i \Delta\mathcal{U}^{(i)}L^d = \sum_j \sigma_s\Delta\epsilon^{(j)}L^d, \tag{3.2}$$

where the sum on the left is over all energy drops, and the sum on the right is over all elastic loading segments, which are equal in number.

As shown in Figs. 2.2, 3.7 and 3.8 there is also a well defined steady-state shear stress. Thus we can rewrite Eq. 3.2 as

$$\sum_i \Delta\mathcal{U}^{(i)}L^d = \langle\sigma_s\rangle\sum_j \Delta\epsilon^{(j)}L^d, \tag{3.3}$$

introducing corrections proportional to the square of stress fluctuations, which go to zero as $L^{-2\phi}$ in the thermodynamic limit (Table 3.1). A steady state shear stress also implies that the stress rises during elastic loading balance the stress drops during avalanches over long strain intervals. The stress rise over each elastic interval j can

be written as $\mu\Delta\epsilon^{(j)}$ where μ is the shear modulus, so that:

$$\sum_i \Delta\sigma^{(i)} L^d = \sum_j 4\mu\Delta\epsilon^{(j)} L^d. \tag{3.4}$$

Other workers have found that above a length scale smaller than our system sizes variations in the modulus μ between different elastic segments are small (Tsamados et al., 2009).

Combining the relations above with the definitions of S and E allows us to relate total stress and energy drops

$$\sum_i S^{(i)} = \sum_i E^{(i)} \tag{3.5}$$

Since the summations are over the same set of avalanche events this also implies that the mean values are equal $\langle S\rangle = \langle E\rangle$.

The sum rule in Eq. 3.5 only constrains the mean value or the sum over all events, but one might expect that something similar to the principle of detailed balance leads to a correlation between E and S for individual events. This correlation clearly breaks down for small events. Indeed, while E is always positive, S can have either sign for small events (Lerner and Procaccia, 2009). Large events dominate the sums in Eq. 3.5 and their energy and stress drops are more strongly correlated.

3.2 Stress Energy Relation

Figure 3.2 shows how the mean and variation in S for events of a given E change with avalanche size. Results are normalized by E to accentuate deviations from linear

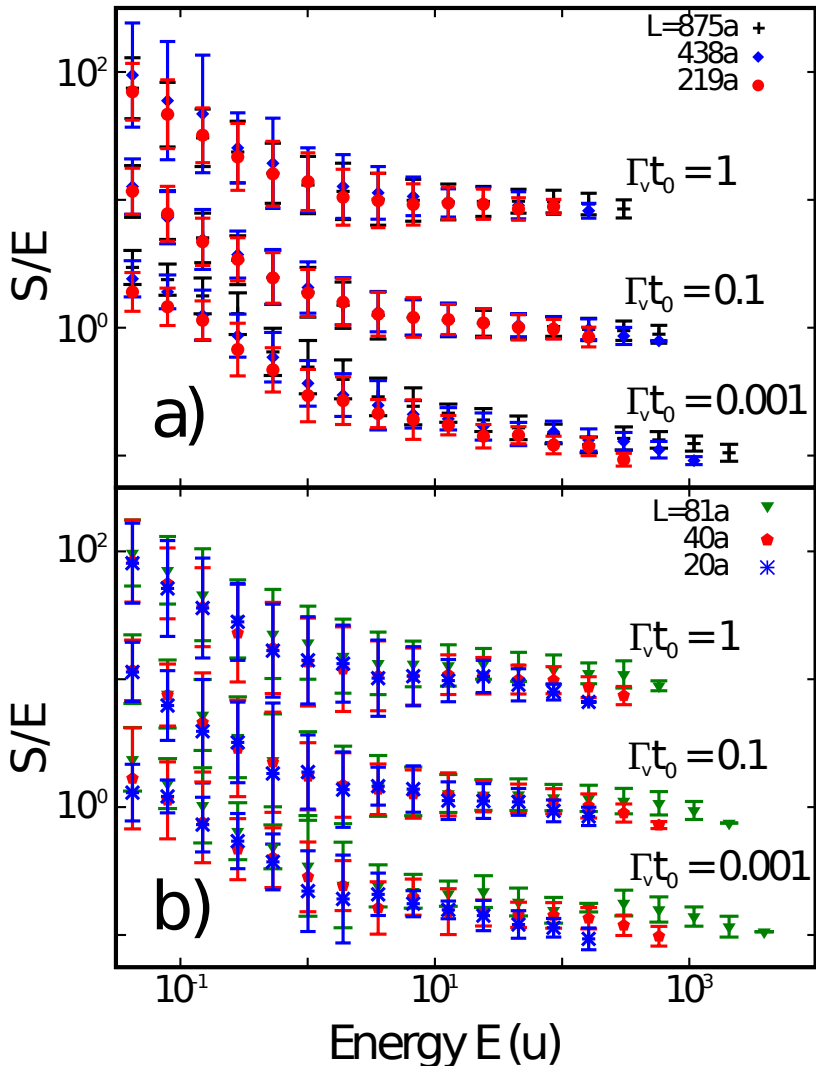

Figure 3.2: The ratio of mean stress drop to energy drop, S/E, of avalanche events for a) two-dimensional and b) three-dimensional systems, binned by logarithm of energy. To prevent overlap, results for overdamped and underdamped systems are multiplied by 10 and 0.1, respectively. Error bars indicate the spread in stress drop for avalanches of a given energy. A linear relationship between S and E holds for $E \gtrsim 1 - 4u$ for the overdamped and crossover damping.

behavior and results from different damping rates are offset to prevent overlap. For energies less than a crossover energy the stress drop is much larger than E and has large fluctuations. In the overdamped regime this crossover occurs between $1-2u$ for both two and three dimensions, while for the crossover damping regime we estimate the crossover energy to occur between $2-4u$. The presence of large fluctuations and occasional negative drops suggests that events smaller than the crossover energies do not necessarily contribute to a release of the imposed shear stress. For energies larger than the crossover energy the mean stress drop is nearly equal to E for the overdamped and crossover damping cases. Only these larger events exhibit critical scaling for both E and S. Fig. 3.2 implies that E and S should have the same scaling exponents in this regime.

In the underdamped limit, S/E only approaches unity for the largest events, which move to larger E as L increases. The sum rule is not violated, but the scaling of avalanches with E and S may be different. The data can be fit to a power law $S \sim E^{\eta}$ with $\eta \approx 0.9$ over the range $5u < E < 2000u$, but the prefactor must be L dependent so that $S/E \to 1$ at the largest events. The deviation from linearity is a natural result of reduced damping and inertia. In the overdamped limit there should be a correspondence between stress and potential energy, as traversing each potential energy barrier dissipates energy. In the underdamped limit potential energy barriers may be surmounted with little energy dissipation, leading to decoupling of the dissipated energy and the stress drop. The implications of this decoupling are

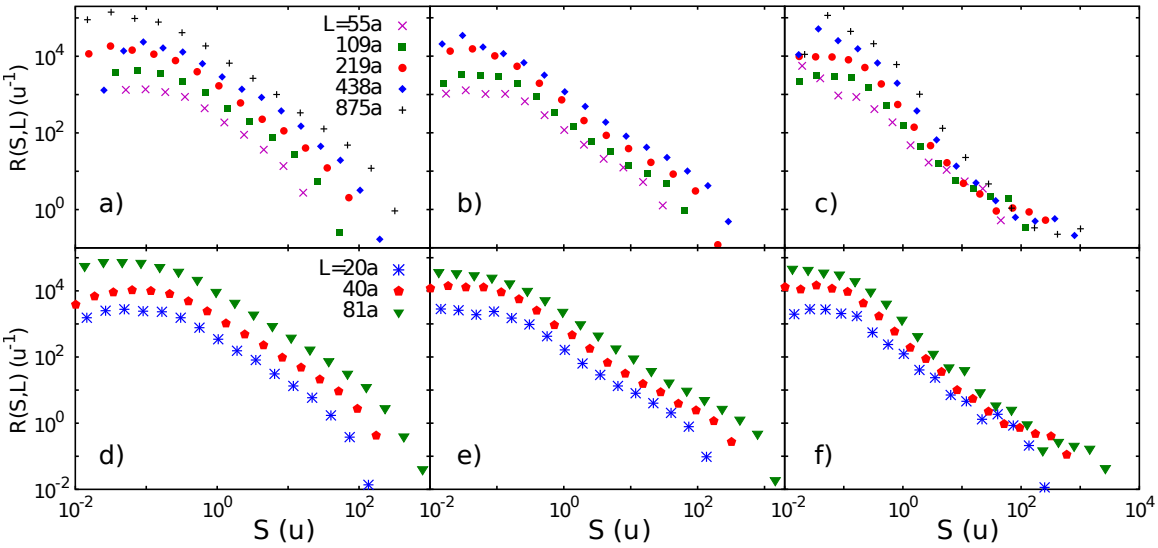

Figure 3.3: Unscaled distribution of stress drops, $R(S, L)$ in two dimensions for damping rates a) $\Gamma_v t_0 = 1$, b) $\Gamma_v t_0 = 0.1$, and c) $\Gamma_v t_0 = 0.001$, and in three dimensions for d) $\Gamma_v t_0 = 1$, e) $\Gamma_v t_0 = 0.1$, and f) $\Gamma_v t_0 = 0.001$. System sizes range from $L = 55a$ to $875a$ in two dimensions and $L = 20a$ to $L = 81a$ in three dimensions. The curves shift up and to the right with increased system size, indicating that both the rate of events and the size of the largest events increase with system size in all cases.

discussed further in the section on finite-size scaling.

3.3 Avalanche Distributions

To characterize the different universality classes associated with the three damping regimes we examine the behavior of the avalanche rate distribution. To form this distribution we count the number of avalanche events with energy drop E or stress drop S during a given strain interval. We define the rate of events as the number of events per unit strain and energy of a given energy $R(E, L)$ or stress drop $R(S, L)$.

Raw $R(S, L)$ distributions for the three damping regimes in two and three di-

mensions are shown in Fig. 3.3. As expected, the number of events of a given size increases with system size in all cases. If the density of avalanche nucleation sites were independent of system size one would expect $R(S, L)$ to scale with the number of particles, *ie* as L^d, for small S. Many previous studies of avalanche behavior, for example in interface depinning, have found or assumed this extensive scaling (Fisher, 1998; Martys et al., 1991b; Stauffer and Aharony, 1994). In contrast, we find subextensive scaling in the avalanche rate distribution for all damping rates in both two and three dimensions.

3.3.1 Rates of Small Events

Figure 3.4 shows $R(S, L)$ and $R(E, L)$ scaled by L^γ with γ chosen to collapse the distributions for E and S within the critical scaling range. For different geometries and damping rates both $R(S, L)$ and $R(E, L)$ follow a power-law dependence on avalanche size from $\sim u$ up to a maximum size that grows with system size. Note that the nature of the cutoff at large avalanche sizes varies with damping rate. There is a simple rapid decay in the number of large events for the overdamped and crossover cases. For the underdamped case there is an excess of large events that leads to a plateau before the distribution cuts off.

We have shown in Fig. 3.2 that avalanches with energy drop smaller than a crossover energy differ from larger avalanches. The distributions $R(S, L)$ and $R(E, L)$ also differ below this scale and only follow critical scaling for larger events. For

underdamped systems $R(E, L)$ and $R(S, L)$ both show L dependent saturation below $E \sim 0.3u$ and $S \sim 2u$, respectively. For overdamped and crossover systems $R(S, L)$ saturates for $S \lesssim 0.1$ while $R(E, L)$ continues to rise as a power law as E decreases. At the crossover damping, $R(E, L)$ follows a single power law up to the size dependent cutoff. For overdamped systems there is a change in power law at $E \sim u$. The exponent for small avalanches is less than unity and varies with system size. Previous simulations have also observed this regime, but were too small ($L \lesssim 50a$) to see the critical scaling at large E. Note that $L = 55a$ results are cut off by system size at $E \gtrsim 8u$, giving less than a decade of scaling.

Table 3.1 lists the values of γ that give the best collapse of $R(E, L)$ and $R(S, L)$ in the critical scaling region from the crossover energy to the upper cutoff. Quoted uncertainties indicate where deviations between curves for different L differ by more than the statistical errors, which are comparable to the symbol size. As noted above, γ is substantially less than d in all cases. This represents a breakdown of hyperscaling that is tied to the growth in the size of the largest events with L. These larger avalanches either reduce the probability that a given region can nucleate small events, or increase the probability that a nucleation site will produce a larger avalanche. The size of the largest avalanches increases with decreasing Γ_v and there is a corresponding drop in γ.

Note that for the overdamped regime the stress distribution shows a larger scaling range in Fig. 3.4, while in the crossover and underdamped regimes the energy drop

shows a larger range of power-law behavior. The deviation in behavior of S and E comes from the regions where $S/E > 1$ in Fig. 3.2. This region extends to larger E as L increases for underdamped systems. There is a corresponding shift to larger S in the start of the scaling regime in $R(S, L)/L^{\gamma}$.

Given the above observations, the most accurate exponents are obtained from $R(S, L)$ in overdamped systems and $R(E, L)$ for crossover and underdamped systems. The difference is only significant for the underdamped case. The solid lines in Fig. 3.4 show power-law fits $R(\chi, L) \sim \chi^{-\tau}$ with τ given in Table 3.1 and $\chi = S$ for overdamped systems and $\chi = E$ for other cases. Parallel lines are drawn near $R(E, L)$ for overdamped systems and $R(S, L)$ for other cases. The results are consistent with power-law scaling in the critical region, but the exact region over which the slope of the distributions should be fit is difficult to determine using this figure. As in other critical systems, finite-size scaling of results for different L provides a better method for determining the range of critical scaling for the avalanche rate distribution (Privman, 1990; Perković et al., 1999).

3.3.2 Finite-Size Scaling

The assumption underlying the finite-size scaling procedure is that rather than depending separately on S or E and L, the avalanche rate distributions are a function only of the ratio of avalanche size to a power of the system size (Privman, 1990). They

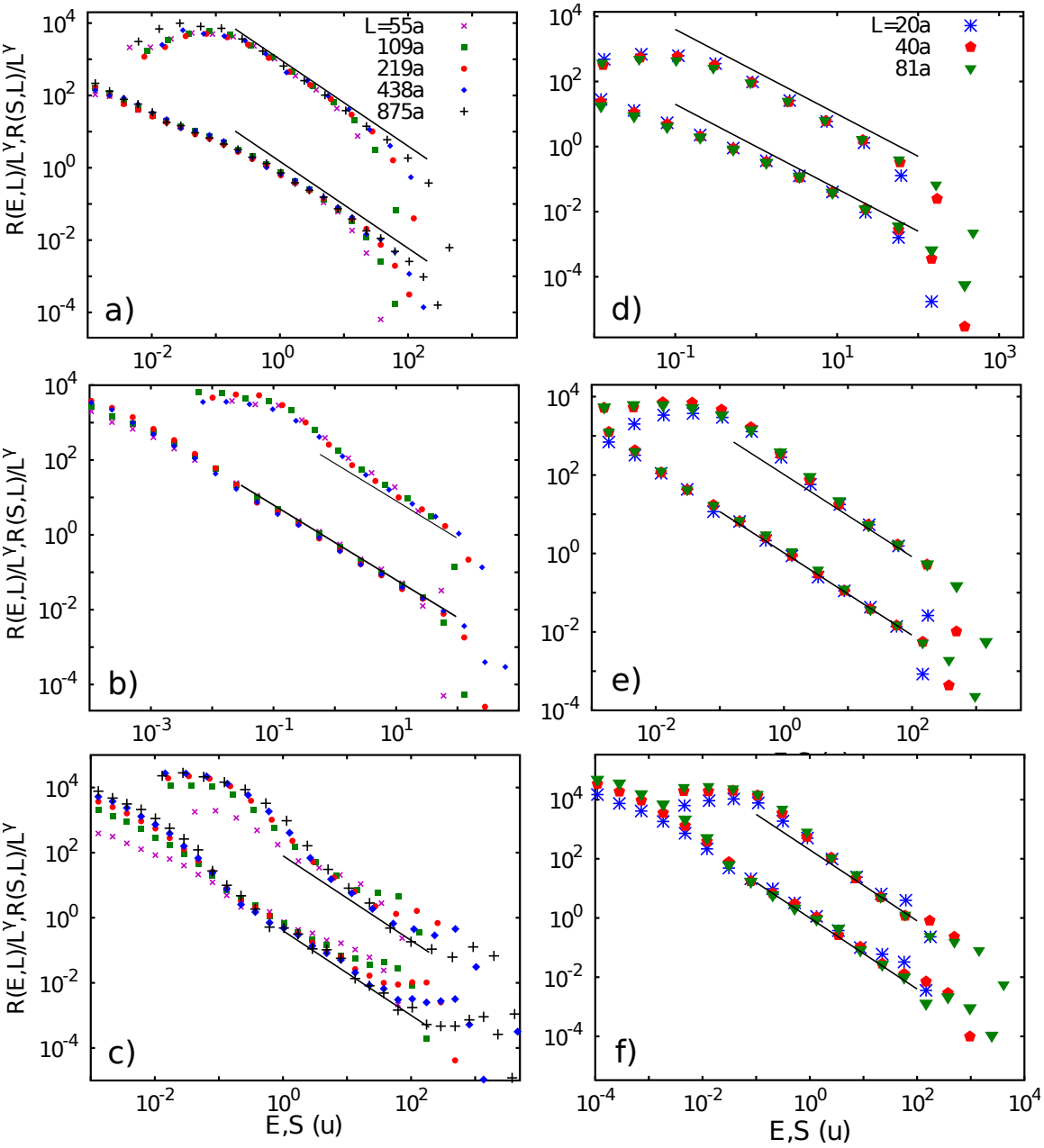

Figure 3.4: $R(S,L)$ and $R(E,L)$ avalanche rate distributions scaled by L^{γ} for the two-dimensional a) overdamped ($\Gamma_v t_0 = 1$), b) crossover ($\Gamma_v t_0 = 0.1$), and c) underdamped ($\Gamma_v t_0 = 0.001$) regimes and in three dimensions for the d) overdamped ($\Gamma_v t_0 = 1$), e) crossover ($\Gamma_v t_0 = 0.1$), and f) underdamped ($\Gamma_v t_0 = 0.001$), regimes. In all cases the distribution of stress drops $R(S,L)$ is plotted above the distribution of energy drops $R(E,L)$ and lines of slope τ are drawn next to each distribution. Values of γ and τ for each system are given in Table 3.1. Values of γ are chosen to collapse the distributions for different system sizes for avalanche events in the scaling range.

then obey the scaling ansatz

$$R(\chi, L) = L^{\beta} g(\chi / L^{\alpha}), \tag{3.6}$$

where χ is either E or S and $g(x)$ is a scaling function that depends on damping rate Γ_v and may be different for E and S. The scaling function decays to zero at large arguments so that there are few avalanches above a largest size χ_{max} that increases with system size as L^{α}. Given the assumption that no smaller energy or length scales are important, $g(x)$ must scale as a power law at small arguments:

$$g(x) \sim x^{-\tau} \quad , \quad x << 1. \tag{3.7}$$

As shown above, the number of avalanches of a given size χ scales as L^{γ} for $\chi < \chi_{max}$. Combining equations 3.6 and 3.7 gives

$$R(\chi, L) = L^{\beta} g(\chi / L^{\alpha}) \sim L^{\beta + \alpha\tau} \chi^{-\tau}. \tag{3.8}$$

This gives us our first scaling relation between exponents,

$$\gamma = \beta + \alpha\tau. \tag{3.9}$$

Another scaling relation can be derived from energy balance in steady state. The total work per unit volume per unit strain is just the mean stress $\langle \sigma_s \rangle$. Equating the total work done in the entire system to the sum of energy drops in all avalanches one finds:

$$\int R(E, L) E dE = \langle \sigma_s \rangle L^d. \tag{3.10}$$

Γt_0	d	τ	α	γ	ϕ
1.0	2	1.3 ± 0.1	0.9 ± 0.05	1.3 ± 0.1	1.00 ± 0.1
0.1	2	1.0 ± 0.05	0.8 ± 0.1	1.2 ± 0.1	0.9 ± 0.1
0.001	2	1.25 ± 0.1	1.6 ± 0.1	0.8 ± 0.1	0.5 ± 0.1
1.0	3	1.3 ± 0.1	1.1 ± 0.1	2.1 ± 0.1	1.5 ± 0.2
0.1	3	1.05 ± 0.05	1.5 ± 0.1	1.6 ± 0.1	1.30 ± 0.1
0.001	3	1.2 ± 0.1	2.1 ± 0.2	1.3 ± 0.2	0.9 ± 0.1

Table 3.1: Scaling exponents determined for overdamped ($\Gamma t_0 = 1$) and underdamped ($\Gamma t_0 = 0.001$) limits and at the crossover regime $\Gamma t_0 = 0.1$ in two and three dimensions. Quoted values satisfy the scaling relation $\gamma = d - (2 - \tau)\alpha$ and errorbars are estimated from the finite-size scaling collapses for E and S. The probability of avalanches decays as $E^{-\tau}$, the largest avalanche scales as L^{α}, the rate of small avalanches scales as L^{γ}, and the range of stresses scales as $L^{-\phi}$.

Inserting the scaling relation and changing variables to $x = E/L^{\alpha}$, one finds:

$$L^{\beta+2\alpha} \int g(x) x dx \sim L^{d}, \tag{3.11}$$

yielding

$$\beta = d - 2\alpha. \tag{3.12}$$

Note that the integral in Eq. 3.11 converges and is insensitive to the lower bound because $\tau < 2$ for all systems. If hyperscaling was obeyed, $\gamma = d$ would imply $\tau = 2$, which is clearly inconsistent with the data.

Figure 3.5 shows finite-size scaling collapses for both the energy and stress drop using the scaling ansatz in Eq. 3.6, with β obeying Eq. 3.12. The exponent α

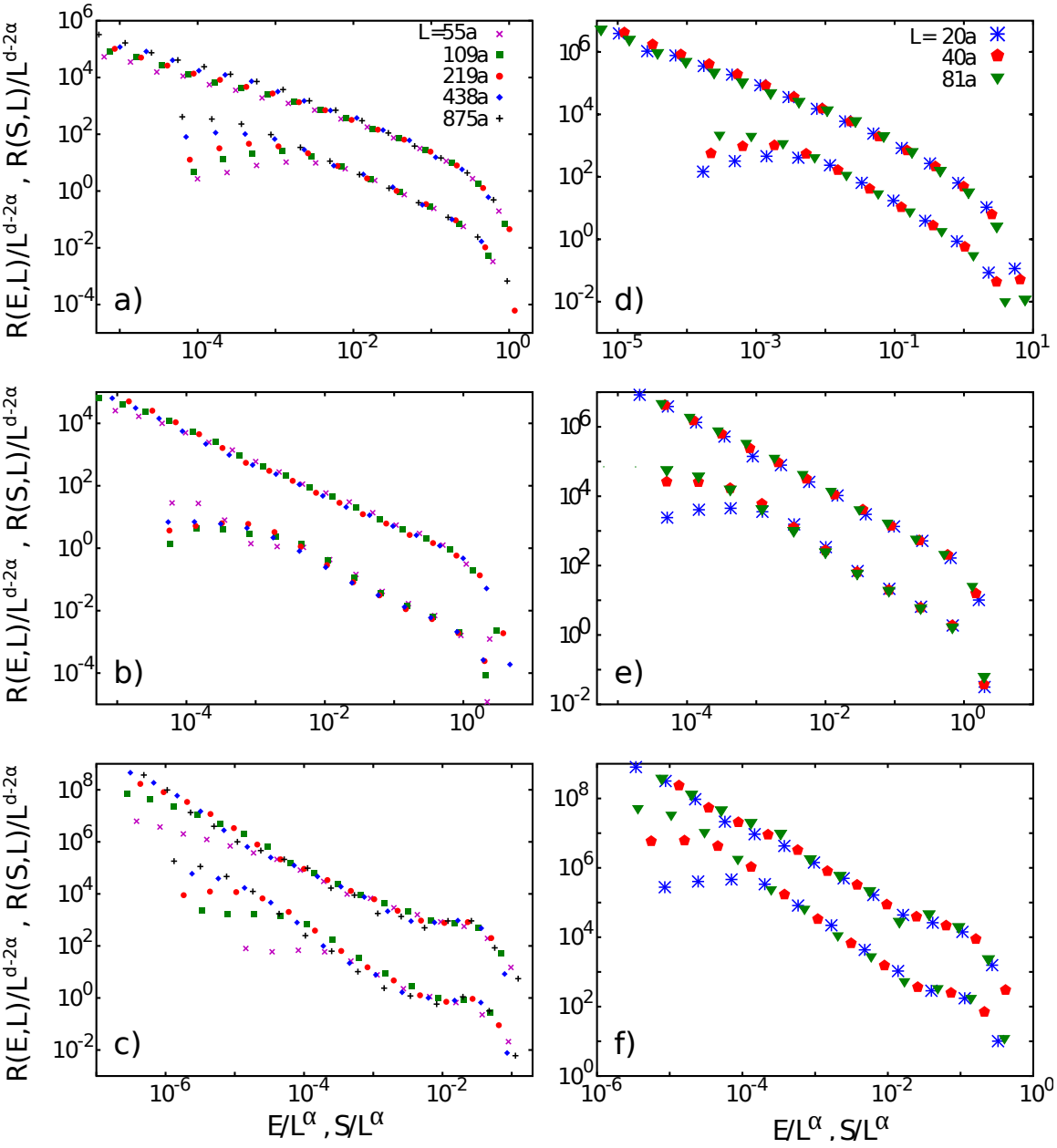

Figure 3.5: Finite-size scaling for $R(E, L)$ and $R(S, L)$ avalanche rate distributions in two dimensions (left) and three dimensions (right) for a),d) overdamped, b),e) crossover, and c),f) underdamped regimes. The value of α used in each collapse is given in Table 3.1 and symbol sizes are comparable to statistical errorbars.

is chosen so that data for large events from different system sizes collapse onto a universal curve that corresponds to the scaling function $g(\chi/L^{\alpha})$. In all cases the curves deviate from the scaling function at a scaled energy $E \sim u/L^{\alpha}$, which decreases with increasing L. The energy of a single bond $\sim u$ is a natural discrete energy scale where the assumption of scale invariance underlying Eq. 3.6 breaks down. We also considered collapses where β was allowed to deviate from the scaling relation in Eq. 3.12, but found there was no significant improvement. As with the exponent γ, the uncertainties in the value of α are determined by varying α and finding a range of values over which the collapse is acceptable. This determination utilizes the fact that the symbol sizes in Fig. 3.5 are comparable to the errorbars.

Figure 3.6 shows the finite size scaling collapses for the energy and stress drop distributions $R(\chi, L)$ multiplied by $L^{-\gamma}\chi^{\tau}$ in order to make the curves flat over the range of energies from u to χ_{max}. This presentation is useful in three ways: First, the exponent τ can be estimated by finding the value for which the curves appear flat. Second, the lateral spread in the distribution curves for the different system sizes helps to determine the scaling exponents γ and α. Finally, this form makes apparent the range of scaled energy values which comprise the scaling regime. Outside this regime deviations from a flat collapse become quite noticeable. Values of the exponent τ used in these figures are listed in Table 3.1 The uncertainty in the exponent τ is determined from the range of values over which the distributions appear approximately flat. The values of the exponent τ given in Table 3.1 are consistent with the scaling relation

Eq. 3.9 and fit the unscaled data shown in Figs. 3.3, 3.4, and 3.5.

The values of α and τ listed in Table 3.1 reflect scaling exponents measured using our best determination of the critical scaling range. As with the determination of the exponent γ, this could be a source of systematic error in our measurements. In the overdamped regime, fits to $R(S, L)$ give the smallest uncertainty and in the other cases fits to $R(E, L)$ extend over the longest range. Fits to S and E only differ significantly for the underdamped case. The slope of $R(E, L)$ is given in Table 3.1, while the slope of $R(S, L)$ appears larger for both two and three dimensions, closer to $\tau \approx 1.5$ for certain energy ranges. This difference in slope can be explained by the features in Fig. 3.2. Since S and E are not linearly related, their distributions should also differ slightly, with $R(S, L)$ being steeper.

It is clear from the finite-size scaling collapses that dimensionality does not affect the function $g(x)$, but that its form changes with damping rate. The form of $g(x)$ in the underdamped regime is of particular interest. It displays a characteristic plateau at large avalanche sizes in both two and three dimensions. Such an excess of large avalanches is seen in both earthquakes and experiments on sand piles (Scholz, 2002; Held et al., 1990). An excess of system spanning events has also been seen in the Burridge-Knopoff model. In some versions of that model a consistent finite-size scaling collapse was not found because a high-energy peak separated from the lower part of the distribution (Carlson and Langer, 1989; Carlson et al., 1991; Carlson, 1991). In our system there is a plateau rather than a second peak, and the entire distribution

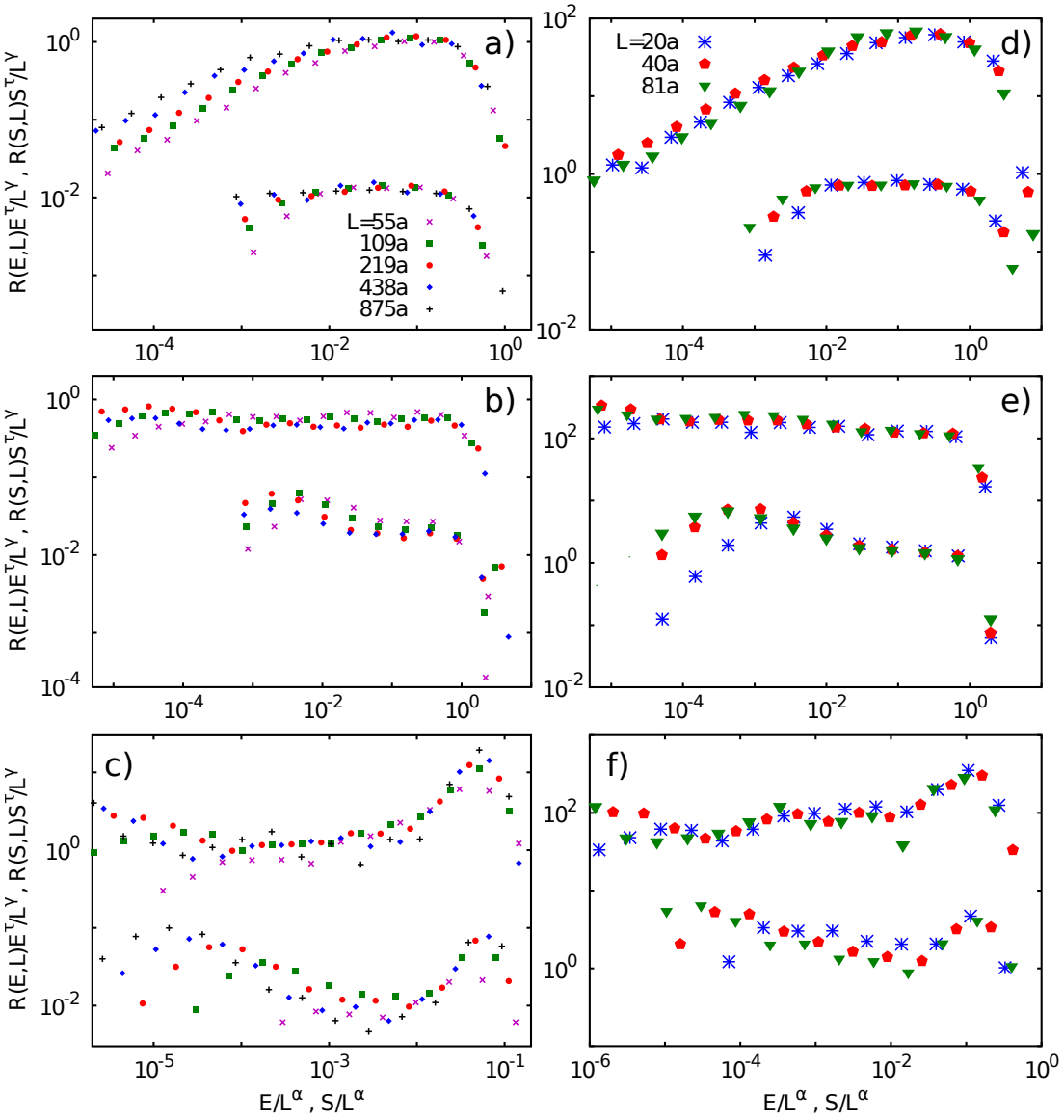

Figure 3.6: Finite size scaling for flattened $R(\chi, L)$ distributions in two dimensions (left) and three dimensions (right) for a),d) overdamped, b),e) crossover, and c),f) underdamped regimes. The distributions have been multiplied by the scaled variable χ^τ to make the distributions flat. In each panel the top set of data corresponds to energy drop $R(E, L)$ while the bottom curve corresponds to stress drop $R(S, L)$. The value of the exponents τ and γ used in each collapse is given in Table 3.1 and symbol sizes are comparable to statistical errorbars.

collapses at large scaled energies.

3.4 Distribution of Stress Values

One of the most basic quantities measured in a deformation simulation or experiment is the stress. In this section we consider the distribution of shear stress values before and after each event, $P(\sigma_s)$. Figure 3.7 shows the distribution of stress values before (closed symbols) and after (open symbols) avalanches for two-dimensional underdamped systems of different size. The distributions narrow about a limiting mean value as the system size increases. If inertia drove the system away from criticality and the onset of shear was a first order transition, one would expect a gap between the distribution of stresses before and after avalanches. There is no evidence of this separation in our results. Even as they narrow, the distribution of stresses before and after avalanches continue to overlap. For all cases considered, the shift between the two distributions is much smaller than their width. In the following we use the distribution of all instantaneous stress values at constant strain rate in order to improve the statistics in two dimensions. In three dimensions the statistics for the quasi-static simulations are satisfactory and these results are shown.

One way to describe the variation in $P(\sigma)$ with system size is to use a finite-size scaling ansatz similar to Eq. 3.6 above. The shear stress distribution $P(\sigma_s)$ can be

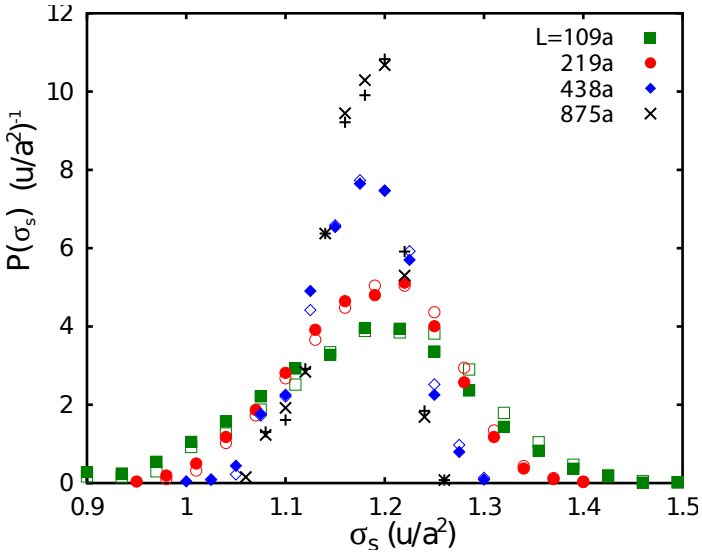

Figure 3.7: The probability distribution for stress values $P(\sigma_s)$ before (open symbols) and after (closed symbols) each avalanche event in the two-dimensional system in the underdamped regime.

rewritten with a scaling function $h(x)$ as

$$P(\sigma_s) = L^{\phi} h(\tilde{\sigma}_s L^{\phi}) \tag{3.13}$$

where $\tilde{\sigma}_s = (\sigma_s - \langle \sigma_s \rangle_L)$, is the stress value with the system size dependent mean stress, $\langle \sigma_s \rangle_L$, subtracted. The width of the distribution around the mean decreases as $L^{-\phi}$ with increasing L. Note that L must enter with the same power inside and outside the scaling function in order to preserve the normalization of the probability distribution.

We confirm the scaling form for the shear stress probability distributions given in Eq. 3.13 by finding values of ϕ which collapse results for the various system sizes and damping rates. Finite-size scaling collapses for two-dimensional finite strain rate simulations and three-dimensional quasi-static simulations are plotted in Fig. 3.8.

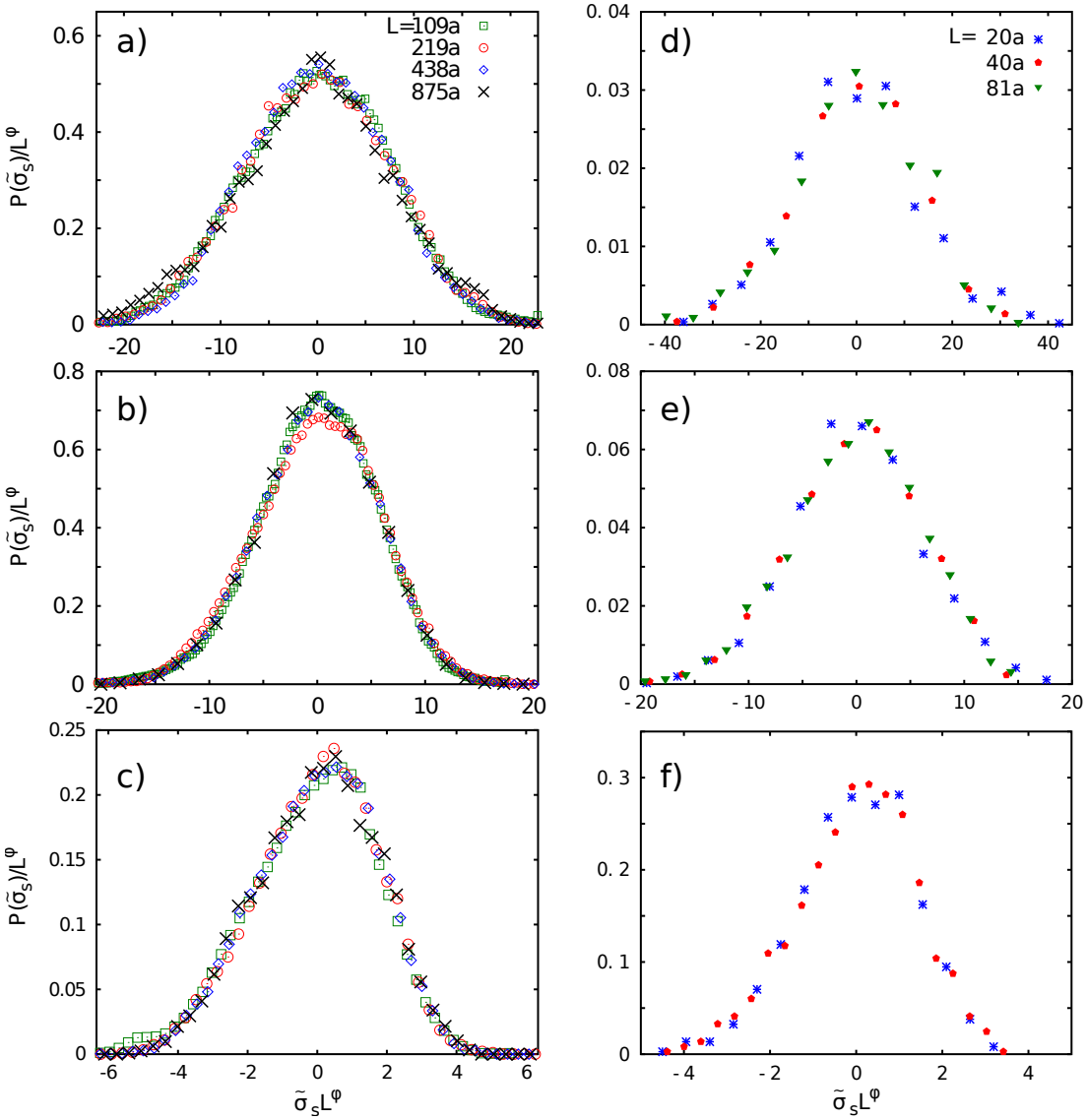

Figure 3.8: The scaled distribution of stress values $P(\sigma_s)$ in two dimensions at finite rate for the a) overdamped, b) crossover, and c) underdamped system. The scaled distribution of stress values is also shown for quasi-static simulations in three dimensions for the d) overdamped, e) crossover, and f) underdamped system. While the mean value is approximately constant for each damping rate, the distribution width scales with system size as $L^{-\phi}$. Values of ϕ are listed in Table 3.1.

The best-fit values of ϕ for all systems simulated are listed in Table 3.1.

Two upper bounds on the value of ϕ may be set. If there were an incoherent addition of stress from different regions with no correlations in time or space, one would expect the width of the distribution to scale as the inverse square root of the number of independent regions (or particles). This yields a relation $\sqrt{\langle(\sigma_s - \langle\sigma_s\rangle)^2\rangle} \sim L^{-d/2}$, or $\phi = d/2$. Correlations could make fluctuations decay more slowly with L, so that $d/2$ is an upper bound for ϕ. The width of the distribution must also be at least as large as the stress change due to the largest avalanches, which are of order $L^{-(d-\alpha)}$. This implies that $\phi \leq d - \alpha$.

The values of ϕ listed in Table 3.1 satisfy the above bounds in all cases in two and three dimensions, and ϕ is comparable to the smallest bound, $\phi \approx min(d/2, d-\alpha)$. The two-dimensional overdamped and critically damped systems have $\phi \approx d/2 \approx d-\alpha$. In three dimensions it is clear that for the overdamped systems $d-\alpha$ is greater than the $d/2$ bound, and $\phi \approx 1.5 = d/2$. Finally, in the underdamped regime $\alpha = 1.6$ in two dimensions and $\alpha = 2.1$ in three dimensions, and in both cases $\phi \approx d - \alpha$. The crossover from $\alpha < d/2$ to $\alpha > d/2$ is equivalent to the crossover from positive to negative β, indicating that the rate of events of size $S_{max} \propto L^{\alpha}$ is decreasing, or the strain interval between such events is increasing. It appears that at this crossover, the events at L^{α} begin to dominate and set the width of the stress distribution.

The conclusion that the largest events can set the width of the stress distribution seems inconsistent with Fig. 3.7. There we found that the distributions of stresses

before events and after events were nearly the same. The resolution of this discrepancy is that most events are small and can occur at any stage of the loading. The mean and standard deviation of the stresses before and after small events are indistinguishable from the global distribution.

For systems with $\alpha < d/2$ even the largest events have a similar distribution. This is evident in Fig. 3.1 for the overdamped case where the largest events are smaller than the spread in stress and occur at all stresses. For the underdamped case Fig. 3.1 is dominated by the large events which seem to have a characteristic scale and time interval. These large events are in the plateau region where the finite-size of the system is important. While they remain the main source of fluctuations in stress for all L, the fractional change in shear stress goes to zero as L increases, because these largest events increase in size more slowly than L^d.

Studies of depinning often control the driving stress rather than the driving rate Fisher (1998); Martys et al. (1991a); Friedman et al. (2012); Alava et al. (2006). There is then a critical exponent ν relating the distance from the critical stress to the correlation length ξ, corresponding to the linear dimension of the largest avalanches: $\xi \sim |\sigma_c - \sigma|^{-\nu}$. While we have performed simulations with constant rate, the fact that the range of stresses scales as $L^{-\phi}$ suggests that $\nu = 1/\phi$. This relation applies in the limit where the largest avalanches set the range of stress fluctuations, giving $\nu = 1/\phi = 1/(d - \alpha)$. In the case where $\phi = d/2$, stress fluctuations are instead set by uncorrelated fluctuations in the local properties of the system. As pointed out by

Pazmandi et al. Pázmándi et al. (1997), $1/\phi$ does not correspond to the intrinsic ν for the correlation length in this case.

Chapter 4

Energy Dissipation and Dynamics

This chapter compares alternate particle damping mechanisms in order to test the generality of the critical behavior found in Chapter 3. Although critical behavior has been observed for a variety of particle interactions and damping mechanisms the focus of this chapter is on the particular Galilean-invariant damping mechanism described in Chapter 2. This dissipative mechanism has been used in the past (Lemaître and Caroli, 2009; Maloney and Robbins, 2009; Hoogerbrugge and Koelman, 1992), however not with the specific aim of studying the critical behavior observed in the quasi-static limit.

This chapter focuses on the Galilean-invariant damping mechanism because it provides an illustration of both universal and non-universal aspects of the critical behavior. Basic differences in the two models explain some aspects of the overdamped and underdamped limits.

4.1 Avalanche Distributions

As in Chapter 3 above, we examine the avalanche rate distributions $R(S, L)$ and $R(E, L)$ in the overdamped limit, the underdamped limit, and in the crossover regime for the Galilean-invariant dissipative mechanism. In particular we measure the log-log slope of the power-law distribution, τ, and perform finite-size scaling to quantify changes in the avalanche rate distribution with system size through the scaling exponents α and γ. The finite-scaling procedure uses the scaling ansatz

$$R(\chi, L) = L^{d-2\alpha} g(\chi / L^{\alpha}) \tag{4.1}$$

in order to determine the scaling exponent α. Values of α, γ, and τ determined for the Galilean-invariant dissipation mechanism can be compared with values from the viscous damping mechanism to test whether behavior in each regime is the same independent of the dissipative mechanism. Here we perform finite-size scaling for systems with $L = 55a$ to $L = 438a$ or $L = 219a$. This is a smaller range of system sizes than in Chapter 3. This does not allow as precise a determination of the critical exponents as in the case of the viscous damping. Though exponent values are determined with errorbars, the main goal of the comparison is to identify whether behavior is consistent or inconsistent with the previous results.

4.1.1 Overdamped and Underdamped Limits

In the overdamped and underdamped limits there is good agreement between measured exponents for the viscous and Galilean-invariant damping mechanisms. Rate distributions for the overdamped limit are shown in Fig. 4.1a). A finite-size scaling collapse is shown using a common scaling exponent of $\alpha = 0.9$ for both the viscous (open symbols) and Galilean-invariant (closed symbols) damping. For each damping mechanism the top curve corresponds to the distribution $R(S, L)$ while the lower corresponds to $R(E, L)$. Lines of slope $\tau = 1.25$ have been drawn next to each set of curves. This value of τ is our best estimate of the slope of the distribution based on the viscous damping mechanism from Chapter 3 in Table 3.1. The slope of the line matches the distributions for the Galilean-invariant dissipation indicating that τ is consistent between the two dissipation mechanisms. The collapse of the data shows that the scaling exponent α is also the same, independent of damping mechanism in the overdamped limit.

Similarly, Fig. 4.1b) shows that a finite-size scaling collapse in the underdamped limit for both the viscous and Galilean-invariant damping mechanism can be performed using a common scaling exponent $\alpha = 1.55$. This value is between the best exponents determined for each dissipative mechanism and is within the errorbars from both. The collapse appears good for both distributions in part because statistical errors are quite large in the underdamped limit. The line of slope 1.25 drawn next to each distribution indicates that τ also consistent for the two damping mechanisms.

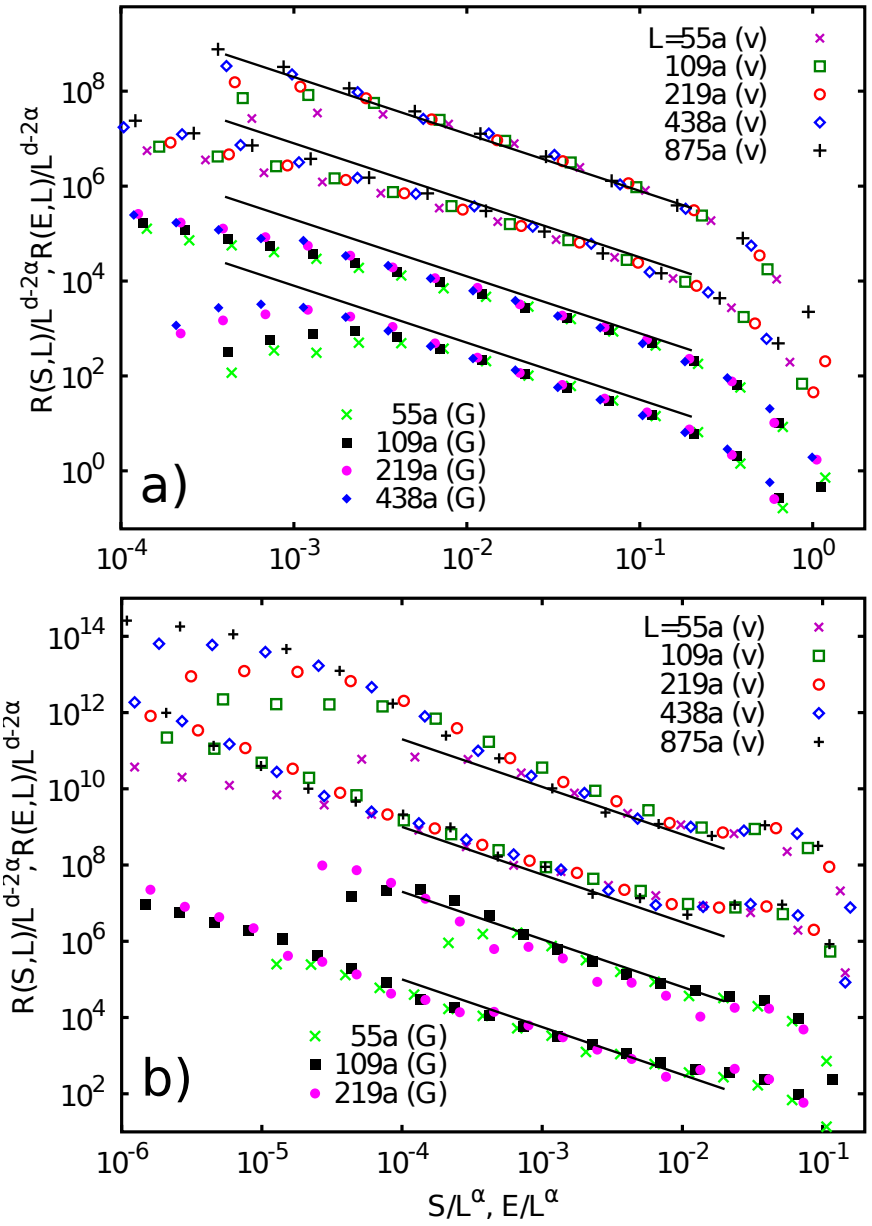

Figure 4.1: Finite-size scaling of $R(S,L)$ and $R(E,L)$ distributions comparing the Galilean-invariant (G) and viscous (v) dissipation in the a) underdamped and b) overdamped limits. The collapse for the different dissipation mechanisms is quite good, with a common exponent $\alpha = 1.55$ in the underdamped limit, and $\alpha = 0.90$, in the overdamped limit. System sizes are indicated. The slope τ has been drawn reflecting the exponent determined for the viscous damping in Chapter 3.

Considering both panels, Fig. 4.1 indicates that both the overdamped and underdamped limits are consistent between the two damping mechanisms. Both the scaling exponent α and the distribution slope τ agree for the two different dissipation mechanisms. This seems to indicate that, independent of the type or nature of the damping applied, the overdamped and underdamped limits have the same universal behavior.

4.1.2 Crossover Damping

In the Galilean-invariant systems the crossover from low to high damping shows different behavior from the viscous damping. Figure 4.2 shows a finite-size scaling collapse for the crossover regime for both the viscous damped and Galilean-invariant damped systems. As in Fig. 4.1 the top two curves correspond to the viscous damping while the bottom two curves correspond to the Galilean-invariant system. The top curve in each pair corresponds to $R(S, L)$ while the lower corresponds to $R(E, L)$. The lines drawn next to each distribution reflect a slope of 1.05, the value of τ determined for the crossover damping.

Though all four distributions have a common slope there is a striking difference in the scaled cutoff between the viscous damped systems and Galilean-invariant systems. This difference is a result of the dramatically different α scaling exponent used to scale the distributions from the two different damping mechanisms. While the viscous damping exponent $\alpha_v = 0.9$ is close to the overdamped value, the value that

collapses the Galilean-invariant curves $\alpha_G = 1.3$ is much closer to the value for the underdamped limit.

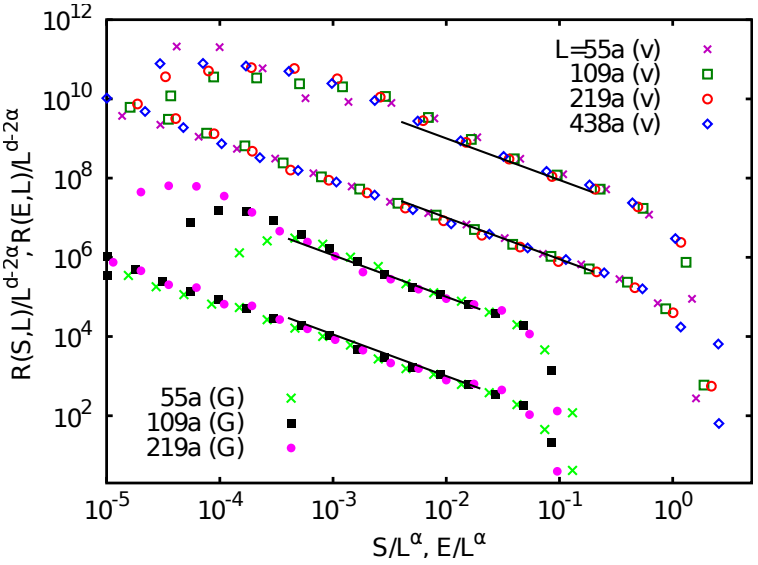

Figure 4.2: Comparison of the finite-size scaling of the avalanche rate distributions $R(S, L)$ and $R(E, L)$ for the Galilean-invariant and viscous dissipation in the crossover damping regime. Scaling exponents measured for the Galilean-invariant (bottom curves) and viscous damping (top curves) $\alpha = 1.3$ and $\alpha = 0.9$ respectively, do not agree with one another. The lines drawn reflect the values of τ listed in Table 3.1.

We can confirm the different behavior of the two damping mechanisms by measuring the exponent γ found in Chapter 3. Figure 4.3 shows avalanche distributions for $R(S, L)$ (open symbols) and $R(E, L)$ (closed symbols) in the a) overdamped limit, b) crossover regime, and c) underdamped limit. The exponent γ used in the collapse are 1.3, 0.8, and 0.8 respectively. In each of the three cases the exponents satisfy the relation $\gamma = d - 2\alpha + \alpha\tau$. This result confirms the finding above that for the Galilean-invariant crossover regime the exponent α is closer to the value of the underdamped limit.

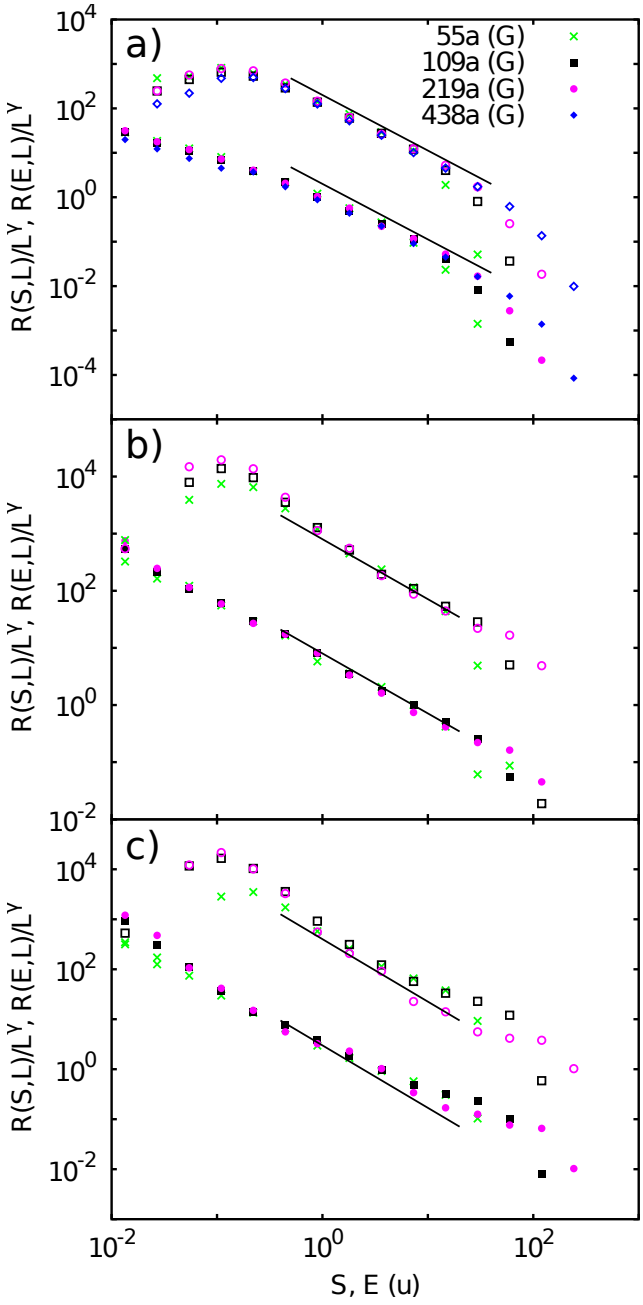

Figure 4.3: Scaling collapses of $R(S, L)$ (open symbols) and $R(E, L)$ (closed symbols) showing the exponent γ for the Galilean-invariant dissipation mechanism. Damping rates correspond to the a) overdamped limit, b) crossover damping, and c) underdamped limit. Values of the exponent γ are given in Table 4.1. While the overdamped and underdamped limits agree with viscous damping results, the crossover value does not. The value, $\gamma = 0.8$, is consistent with the underdamped regime.

Γ_G	τ	α	γ
8.0	1.25 ± 0.1	0.9 ± 0.1	1.3 ± 0.1
0.3	1.05 ± 0.1	1.3 ± 0.1	0.8 ± 0.1
0.05	1.2 ± 0.2	1.5 ± 0.2	0.8 ± 0.2

Table 4.1: Scaling exponents determined for overdamped ($\Gamma_G t_0 = 8.0$) and underdamped ($\Gamma_G t_0 = 0.05$) limits and at the critical crossover between them $\Gamma_G t_0 = 0.3$ for the Galilean-invariant damping mechanism. Quoted values satisfy the scaling relation $\gamma = d - (2 - \tau)\alpha$ and errorbars are estimated from the finite-size scaling collapses for E and S. Exponent values in the limiting damping regimes are consistent with values for the viscous damping mechanism listed in Table 3.1. Exponents for the crossover regime differ substantially.

One simple way to measure the scaling exponent α is to calculate a ratio of consecutive moments of the avalanche rate distribution $\langle E^{n+1} \rangle / \langle E^n \rangle$. Because the exponent τ is greater than one, the normalization of the $n = 0$ moment depends on the small-scale cutoff or avalanche identification criteria. It is generally simplest to use the $n = 1$ moment ratio instead

$$\frac{\langle E^2 \rangle}{\langle E \rangle}. \tag{4.2}$$

Figure 4.4 shows the scaled moment ratio $\langle E^2 \rangle / (\langle E \rangle L^\alpha)$ with $\alpha = 0.9$ chosen to match the overdamped value in Fig. 4.4a) for the viscous damping and Fig. 4.4b) for the Galilean-invariant damping. The value of $\alpha = 1.6$ is chosen match the underdamped limit and collapse the small Γ_v viscous damping data in Fig. 4.4c) and the value $\alpha = 1.5$ is chosen to match the small Γ_G Galilean-invariant damping data in Fig. 4.4d). Considering the top two panels, the overdamped values of α seem to

collapse the data in the high-Γ limit on the right sides of Figs. 4.4a) and b). Likewise, in the bottom two panels the underdamped values of α appear to collapse the data in the low-Γ limit on the left sides of Figs. 4.4c) and d). The dissimilarity between Figs. 4.4a) and b) and Figs. 4.4c) and d) in the intermediate-Γ regime reflects the different scaling exponents for the crossover damping shown in Figs. 4.2 and 4.3.

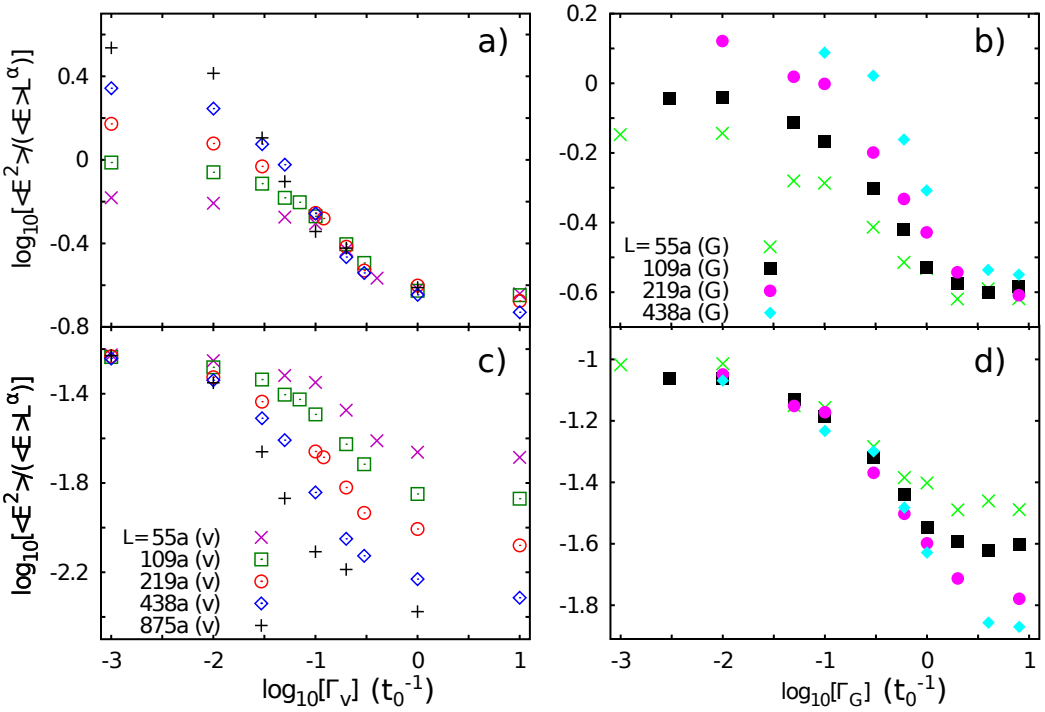

Figure 4.4: The ratio of first to second moment of the energy drop E scaled by the avalanche cutoff $\langle E^2\rangle/\langle E\rangle L^\alpha$. The scaling exponent α is chosen to match the overdamped limit for a) viscous and b) Galilean-invariant dissipation, and the underdamped limit for c) viscous and d) Galilean-invariant dissipation.

The most important distinction between the viscous and Galilean-invariant damping mechanisms can be illustrated by comparing the damping and phonon period timescales. In the analysis that follows we consider timescales for plane waves with wavevector q. For the viscous system there is a simple inverse dependence of the

damping time on the damping rate $\tau_{damp} = 1/\Gamma_v$, independent of wavevector. The Galilean-invariant system has a similar inverse dependence, but there is an additional dependence on wavevector $\tau_{damp} = 1/(k\Gamma_G q^2)$, which produces shorter damping times at short lengthscales. The constant $k \approx 4.5$ takes into account the interaction between the average of ≈ 4 neighbor particles in two dimensions. These damping time scales can be compared with the timescale for the longest and shortest wavelength plane waves in the system: $\tau_{max} \approx L/c$ and $\tau_{min} \approx 2a/c$, where the speed of sound in the system, $c = 3.5a/t_0$. The value $\tau_{min} \approx 0.6$ is about 1.5 times the Einstein period, a measure of of the typical vibrational frequency of a normal mode in the system.

In particular, it is useful to calculate the damping rate required to make all modes in the system overdamped or underdamped. For the Galilean-invariant system all plane waves are underdamped when the shortest wavelength mode ($q = \pi/a$) is underdamped

$$\tau_{damp}/\tau_{min} = ca/(8\pi^2 k\Gamma_G) > 1 \tag{4.3}$$

or $\Gamma_G < ca/(2k\pi^2) \approx 0.2$. For the viscous system, all modes are underdamped when the longest wavelength modes are underdamped, setting the condition

$$\tau_{damp}/\tau_{max} = c/(L\Gamma_v) > 1 \tag{4.4}$$

or $\Gamma_v < c/L \approx 0.004$ for $L = 875a$. Note that this condition depends on the system size, with larger systems requiring lower damping rates. For the viscous damping the overdamped condition is

$$\tau_{damp}/\tau_{min} = c/(2a\Gamma_v) < 1 \tag{4.5}$$

Damping	Overdamped	Underdamped
Viscous	$\Gamma_v > c/2a$	$\Gamma_v < c/L$
Galilean-invariant	$\Gamma_G > cL/k(2\pi)^2$	$\Gamma_G < ca/(k8\pi^2)$

Table 4.2: The overdamped and underdamped conditions for Γ as a function of system size L, and sound velocity c. Relations come from a comparison of the damping timescale, τ_{damp} to mode period $\tau_{max/min}$ of the last mode to become overdamped or underdamped.

or $\Gamma_v > c/2a \approx 1.75$, independent of system size. Conversely, the overdamped condition for the Galilean-invariant damping depends on the longest wavelength mode ($q = 2\pi/L$) and is

$$\tau_{damp}/\tau_{max} = cL/(4\pi^2 k\Gamma_G) < 1 \tag{4.6}$$

or $\Gamma_G > cL/(k4\pi^2) \approx 9$ for $L = 438a$. Note that like the viscous underdamped criterion this condition also depends on system size. These damping limit conditions are summarized in Table 4.2. The above is a simple comparison of timescales. A full analysis of the particle or field equations of motion is more involved, but produces the same system size dependence and only numerical factors differ.

The system size dependence of the damping limits can most easily be seen by examining the dependence of the scaling exponents on scaled damping rate. Figure 4.5 shows the ratio of the first and second moments of the avalanche rate distributions $\langle E^2\rangle/\langle E\rangle$ as in Fig. 4.4. Here the system size-dependent damping limits are shown with the L dependence included. In Fig. 4.5a) the viscous damping data with $\alpha = 1.55$ collapse is shown with the damping rate Γ_v multiplied by L. The data fall on

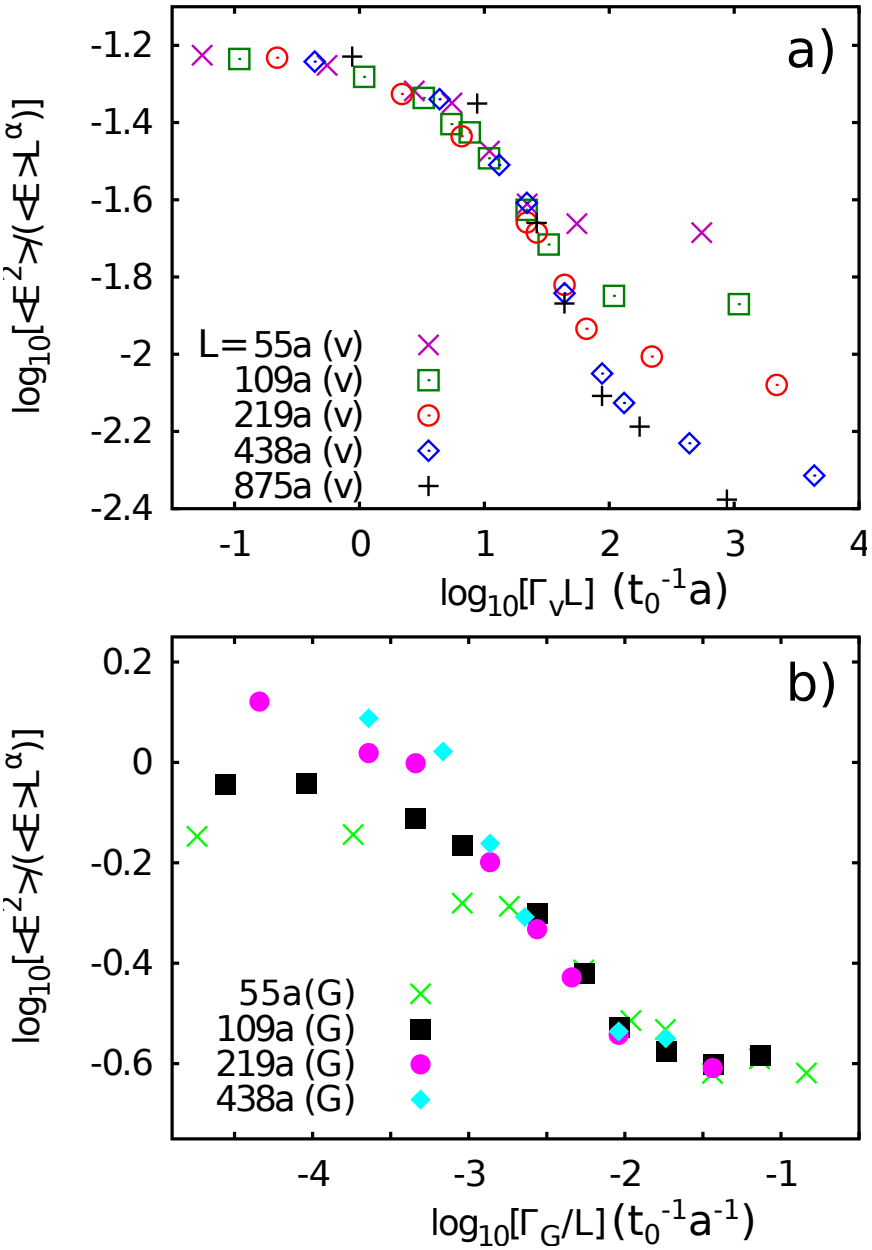

Figure 4.5: The ratio of first to second moment of the energy drop E scaled by the avalanche cutoff $\langle E^2\rangle/\langle E\rangle L^\alpha$ a) in the underdamped limit for the viscous damping and b) in the overdamped limit for the Galilean-invariant system. In a) the viscous damping rate Γ_v has been multiplied by L to show the system size dependence of the viscous underdamped limit. In b) the damping rate Γ_G has been divided by L to show the system size-dependence in the overdamped limit.

a single curve and are consistent with simulations for different values of L scaling in a manner consistent with the underdamped limit at a fixed value of $\Gamma_v L$. Figure 4.5b) shows the overdamped Galilean-invariant damping collapse with $\alpha = 0.9$. The damping rate has been scaled to Γ_G/L as indicated in Eq. 4.6. The data collapse is consistent with systems of different L reaching the ideal overdamped limit at a fixed value of Γ_G/L. Note, the size of the largest event will scale with the exponent α for overdamped systems below this limit.

The system size dependence of the damping limit conditions can be used to infer system behavior in the infinite-system limit. For any viscous damping an infinite-size system will not reach the ideal underdamped limit, as this requires an infinitesimally small damping rate. Conversely, the Galilean-invariant damping is system-size dependent in the overdamped limit, and in the thermodynamic limit the ideal overdamped limit requires infinite damping. Future work will examine the scaling of large events to determine if system size effects change the form of the scaling function or just change prefactors from the asymptotic underdamped and overdamped limits.

In light of the different wavelength dependence of the damping mechanisms, the different crossover behavior exhibited in Figs. 4.2 and 4.4 may be less surprising. In the crossover regime the viscous damping causes the longest wavelength modes to be overdamped while shorter wavelengths are underdamped. For the Galilean-invariant system the converse is true, with the longest wavelength modes underdamped and shorter wavelengths overdamped as the crossover occurs. This different behavior leads

to the different scaling exponents seen in Fig. 4.2. The scaling exponents for the viscous crossover are consistent with the overdamped limit, while exponents for the Galilean-invariant crossover are consistent with the underdamped limit. Evidently the damping of the long-wavelength modes controls the universality class and the scaling exponents exhibited by the system at the crossover damping.

Chapter 5

Plasticity

In contrast to macroscopic experiments and mesoscopic simulations, MD simulations resolve all particle positions and velocities, making it possible to follow and quantify local plastic deformation. There are a variety of ways to define plastic deformation at the particle scale and distinguish plastically deforming regions from surrounding elastic regions (Falk and Langer, 1998; Demkowicz and Argon, 2005; Maloney and Lemaître, 2006; Manning and Liu, 2011). In the past, many computer simulations have examined non-affine displacement fields to look for indications of plastic deformation (Tanguy et al., 2006; Maloney and Lemaître, 2004a; Lemaître and Caroli, 2007). This chapter begins by presenting results which point to a reasonable definition of plastic deformation that correlates well with the overall stress or energy drop of an avalanche.

Results are also presented which track the behavior of the system over large strain

intervals. A strain dependent effective particle diffusion is found, as in previous works. Diffusion shows distinctly different behavior in two and three dimensions. A system size dependence in two dimensions is observed, confirming previous findings (Lemaître and Caroli, 2007; Maloney and Robbins, 2008). The behavior is independent of damping rate, however, a finding that is at odds with previous explanations (Lemaître and Caroli, 2009). System size-independent diffusive behavior is found in three dimensions.

Long-range spatial correlations in deformation found previously are also studied and found to be independent of particle damping (Maloney and Robbins, 2009). Long range correlations are found in strain measures associated with shear deformations but are absent in the volumetric strain invariant. Angular dependence of an invariant related to shear shows weak angular dependence and the vorticity of particle displacement shows strong angular dependence.

5.1 Avalanche Plasticity

5.1.1 Spatial Extent of Avalanches

The goal of this section is to relate the energy or stress drop of an avalanche to the spatial extent of the plastic damage produced the avalanche. This is complicated by the long range of elastic interactions. The simplest type of local shear deformation involving a local rearrangement of a few particles produces elastic strains that decay

as r^{-d} where r is the distance from the particles and d the dimension (Lemaître and Caroli, 2009; Maloney, 2006; Picard et al., 2004; Tanguy et al., 2006). A threshold must be introduced to distinguish these elastic strains from the plastic deformations in the central region. Deviations from the power law decay of strain fields can be used to determine a threshold for distinguishing plastic deformation.

To define strain fields we first find the displacement of each particle during an avalanche. Previous work has emphasized the importance of subtracting any affine component of these displacements that reflects deformation of the box (Tanguy et al., 2006; Maloney and Lemaître, 2004a; Lemaître and Caroli, 2007), but this contribution vanishes in our quasi-static simulations because no strain is imposed during the avalanche. The derivative of the displacement field is calculated by taking a finite difference of displacements on nearby particles. In two dimensions we form a Delaunay triangulation of the particle positions. A linear fit to the displacements of the particles on the corners of each triangle gives $\partial u_i/\partial x_j$, the derivative of the displacement $\mathbf{u}$ along direction i with respect to x_j (Maloney and Robbins, 2008). The symmetrized strain tensor $\epsilon_{ij} = 1/2(\partial u_i/\partial x_j + \partial u_j/\partial x_i)$ is then constructed to eliminate the effect of any translation or rotation of the triangle. In three dimensions, the strain is obtained from finite differences on a tetrahedral tiling.

The magnitude of the strain is usually quantified by rotational invariants. The first, the trace of the strain tensor, measures the magnitude of dilational strains.

Shear is most simply related to the second deviatoric strain invariant J_2. We define

$$\epsilon_d \equiv \sqrt{J_2} = \sqrt{1/2Tr(\overleftrightarrow{\epsilon}^2_{dev})}, \tag{5.1}$$

where $\overleftrightarrow{\epsilon}_{dev}$ is the deviatoric strain tensor $\overleftrightarrow{\epsilon}_{dev} \equiv \overleftrightarrow{\epsilon} - d^{-1}Tr(\overleftrightarrow{\epsilon})\ \overleftrightarrow{I}$. In the case of a simple shear strain ϵ_s in the x-y plane $\epsilon_s = \epsilon_d$. Triangles or tetrahedra with ϵ_d greater than a threshold value ϵ_c are identified as plastic.

In some cases it can be useful to know when triangles have rotated, and in which sense, clockwise or counter-clockwise. In addition to the strain tensor invariants we also examine the vorticity of the displacement field in two dimensions. The vorticity is defined as

$$\omega \equiv \frac{\partial u_y}{\partial x} - \frac{\partial u_x}{\partial y}. \tag{5.2}$$

This measure was used in the past to examine plastic deformation over large strain intervals containing many avalanches, (Maloney and Robbins, 2008) but is also useful in examining individual avalanche events.

The elastic strain field around a localized plastic region decays as a power of the distance r from the region (Lemaître and Caroli, 2009; Maloney, 2006; Picard et al., 2004; Tanguy et al., 2006). The prefactor should be proportional to the magnitude of the plastic rearrangement, which we find scales as the stress or energy drop. Since the spatial arrangements of plastic regions can be complicated, we consider instead the distribution of local strain values $N(\epsilon_d)$. From the scaling of the phase space with distance r, we have $r^{d-1}dr \sim N(\epsilon_d)d\epsilon_d$. Then the distribution of local strains scales

as a power law in two and three dimensions

$$N(\epsilon_d) \sim S\epsilon_d^{-2} \tag{5.3}$$

and the cumulative distribution function (CDF) $N(\epsilon_d > x)$ of strains larger than x scales as:

$$N(\epsilon_d > x) \sim Sx^{-1}. \tag{5.4}$$

Figure 5.1 shows the CDF $N(\epsilon_d > x)$ a) unscaled, and b) divided by avalanche stress drop S. The scaled curves for different avalanche sizes collapse from the large ϵ_d cutoff down to a system and avalanche-size dependent lower cutoff. The $1/x$ form is clear in both figures from the straight line on these log-log plots.

Figure 5.2 shows the average CDF, $N(\epsilon_d > x)$, for avalanche events of a given stress drop S. Events with damping rate $\Gamma_v t_0 = 1$ are shown in Fig. 5.2a), $\Gamma_v t_0 = 0.1$ in Fig. 5.2b), and $\Gamma_v t_0 = 0.001$ in Fig. 5.2c). CDF curves for avalanches binned by energy drop E are shown in Fig. 5.3. Because the interesting features in the distribution are the deviations from elastic response and their dependence on event size, the distributions have been multiplied by the argument x and normalized by the event size, so that the elastic response for an infinite system would predict a collapse onto a horizontal line. Events that are too small to be in the scaling regime do not scale simply with S, but larger events collapse on to a common curve at intermediate x. At small x the CDF is cut off due to finite system size at a value of $x \sim SL^{-2}$ that corresponds to the strain at distances of order the system size.

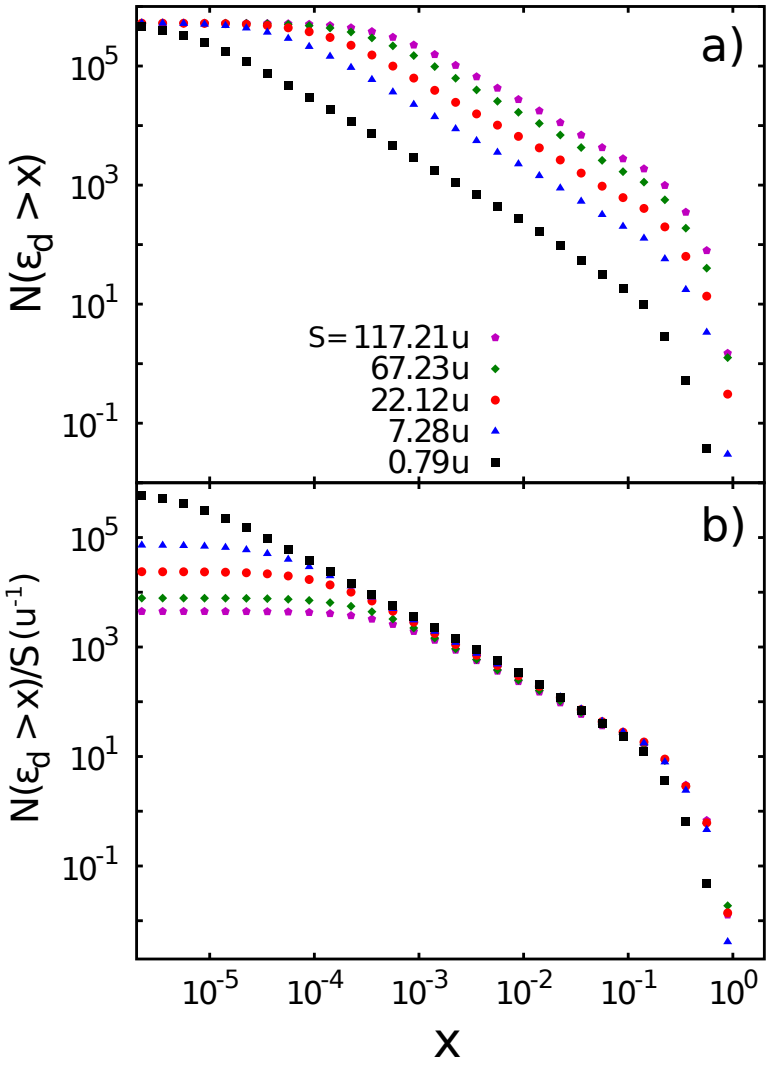

Figure 5.1: The average CDF, $N(\epsilon_d > x)$, of ϵ_d for avalanche events of size S in two dimensions for damping $\Gamma_v t_0 = 1$ and system size $L = 438a$. The a) unscaled distribution and b) scaled distribution both reflect the $1/x$ form of the distribution. The collapse of the scaled distribution indicates that the distribution prefactor is proportional to the avalanche stress drop S.

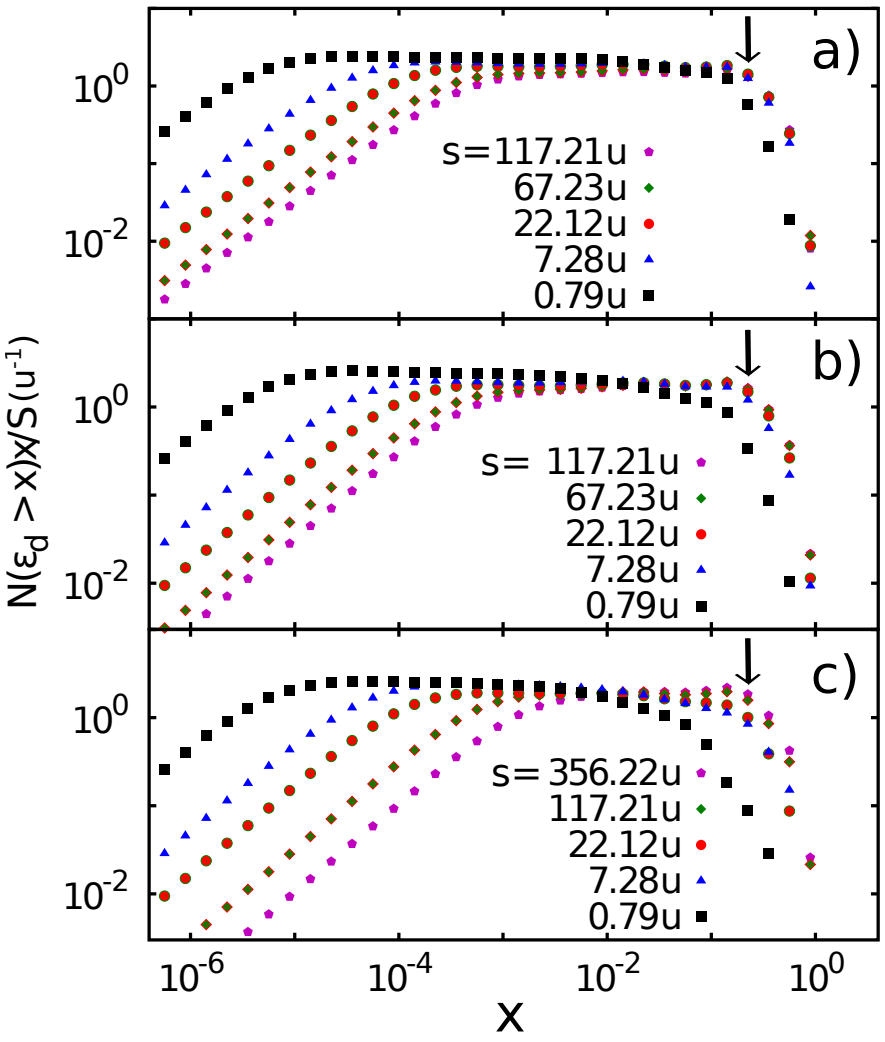

Figure 5.2: The average CDF of ϵ_d for a two-dimensional system of size $L = 438a$ for damping a) $\Gamma_v t_0 = 1$, b) $\Gamma_v t_0 = 0.1$, and c) $\Gamma_v t_0 = 0.001$. In all cases the CDF is multiplied by x/S so that the elastic region should be a constant horizontal line independent of avalanche size. Arrows indicate $\epsilon_c = 0.22$.

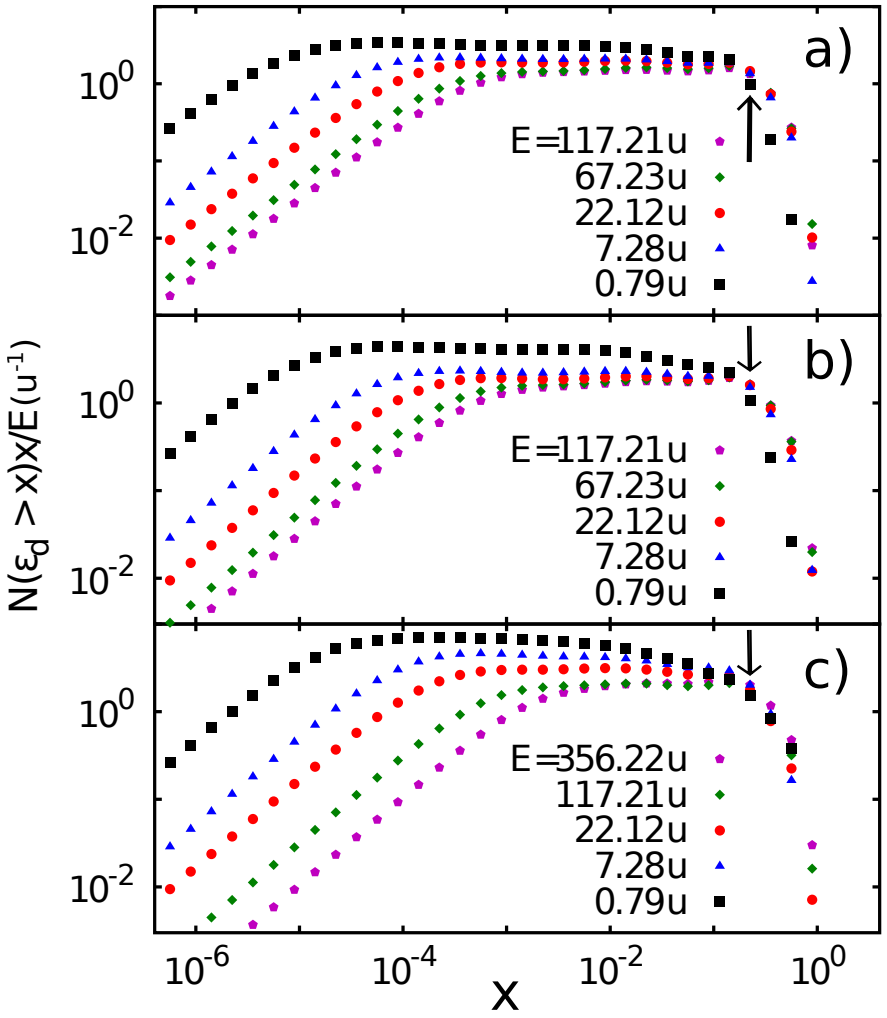

Figure 5.3: The average CDF of ϵ_d for a two-dimensional system of size $L = 438a$ for damping a) $\Gamma_v t_0 = 1$, b) $\Gamma_v t_0 = 0.1$, and c) $\Gamma_v t_0 = 0.001$. In all cases the CDF is multiplied by x/E so that the elastic region should be a constant horizontal line independent of avalanche size. The curves for all damping rates and event sizes in the scaling regime collapse at the critical value of strain $\epsilon_c = 0.22$ (arrow) indicating the number of triangles deforming plastically.

In both two and three dimensions there is a sizeable drop starting between $\epsilon_d = 0.14$ and 0.35. We identify this breakdown of the power-law scaling expected for elastic regions with the onset of plasticity. Regions with ϵ_d greater than $\epsilon_c = 0.22$ are identified as plastic in two and three dimensions. The exact value of this threshold changes quantitative prefactors in the following discussion, but does not affect any of the general conclusions. Note that the CDFs for all events in the scaling regime collapse at $\epsilon_d = 0.22$ in Fig. 5.2. This is consistent with a linear scaling of the number of plastic regions and the stress drop. It is interesting to note that even though the collapse of the elastic tail is only fair for both the stress or energy drop in the underdamped limit the curves collapse at the plastic cutoff for all energy drop sizes and for the largest stress drop sizes.

Based on the results above, we use $\epsilon_c = 0.22$ in both two and three dimensions to indicate plasticity. This is comparable to the ideal elastic limit in dislocation-free crystals. Similar results are obtained with other thresholds and by using the dilational strain. Figure 5.4a shows plots of the number of plastically deformed triangles $N(\epsilon_d > \epsilon_c)$ vs. event size for $\Gamma_v t_0 = 0.1$. The data for energy drop E (open symbols) have been multiplied by 100. Events in the scaling range $(S, E > u)$ show a linear relation between the event size (S or E) and area of the plastic deformation. Data for $\Gamma_v t_0 = 1$ and $\Gamma_v t_0 = 0.001$ are similar.

It is not obvious that the spatial extent and energy of events must be proportional. In particular, larger events could be associated with greater dissipation in each spatial

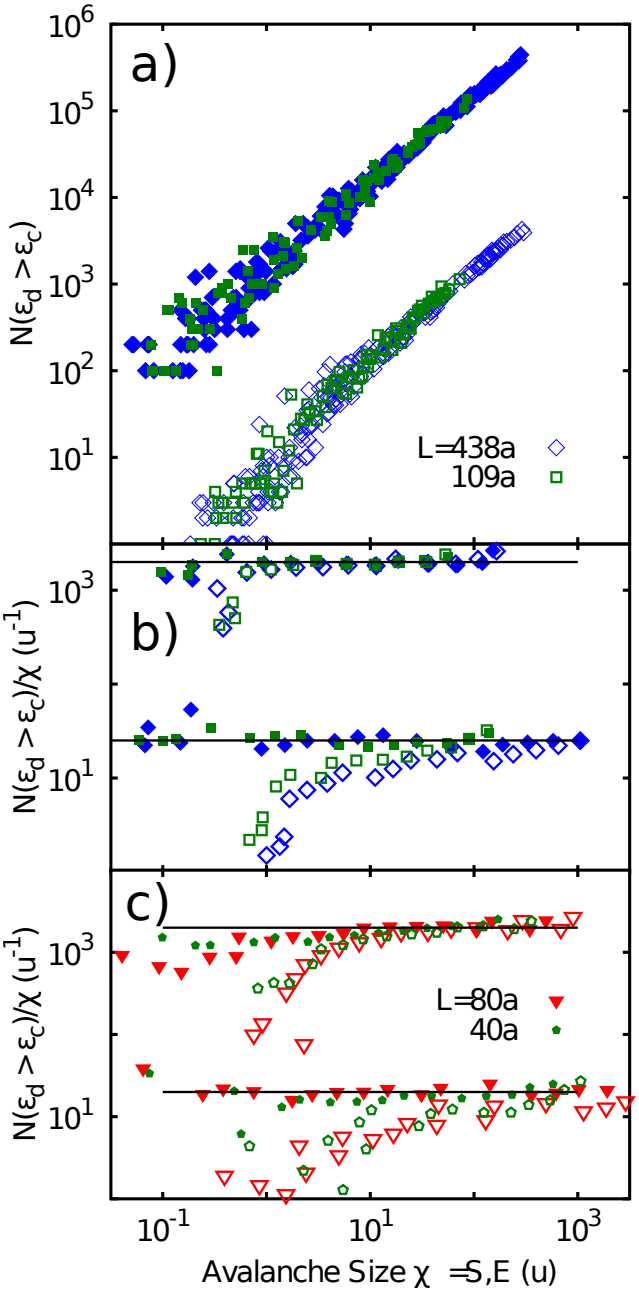

Figure 5.4: (a) The number of plastically deformed Delaunay triangles ($\epsilon_d > 0.22$) during a plastic event versus stress drop S (open symbols) and energy drop E (closed symbols) for two-dimensional systems of the indicated size at crossover damping. Data for E has been multiplied by 100 to prevent overlap. (b) Ratio of number of triangles to mean event size χ with $\chi = E$ (closed symbols) and $\chi = S$ (open symbols) for $\Gamma_v t_0 = 0.001$ and $\Gamma_v t_0 = 1$. (c) Ratio of number of plastically deformed tetrahedra to χ for 3D systems of the indicated size at $\Gamma_v t_0 = 0.001$ and $\Gamma_v t_0 = 1$. Results for $\Gamma_v t_0 = 1$ in (b) and (c) are multiplied by 100 to prevent overlap.

region rather than a spread to new regions. To test this we found the average E or S of events with a given spatial size. Fig. 5.4b shows the ratio of spatial size to mean energy in the overdamped and underdamped limits. Results for different Γ_v are offset to avoid overlap. For the overdamped data the spatial size of systems is proportional to both E and S for events in the scaling region identified in previous sections ($S > 2u$ and $E > 0.3u$). The energy and spatial size are also proportional for the underdamped case. In contrast, results for S only asymptote to a linear relation for the largest events, which grow in size as L increases. This deviation is further evidence that E is the most natural quantity for the finite-size scaling collapses of underdamped systems.

The straight lines drawn in Fig. 5.4b are the best fit for the number of plastically deformed triangles per unit energy. The values are about $20u^{-1}$ for the underdamped systems and $18u^{-1}$ for the overdamped systems. The constant energy dissipation per unit area is consistent with limited local plasticity and local particle displacements during avalanche events. Such behavior was found previously, with total non-affine particle displacements of about one particle radius over strain intervals of about $1/L$ (Maloney and Robbins, 2008). Displacements by a single particle diameter are sufficient to completely change the local forces and thus the shear stress driving further deformation.

Fig. 5.4c shows that the plastically deformed volume also scales linearly with event energy in three dimensions. As in two dimensions, the stress drop in underdamped

systems is less simply related to the plastic volume. The horizontal lines in Fig. 5.4(c) indicate that the number of plastic tetrahedra per unit dissipated energy is about $20u^{-1}$ for all damping rates. This result and the corresponding value for two dimensions explain the limit of the scaling region to energies of order $0.1u$ and above. At $0.1u$ there are only a handful of triangles or tetrahedra that deform plastically. It is natural that the finite size scaling ansatz breaks down and the discreteness of the system becomes important when events involve only a few particles.

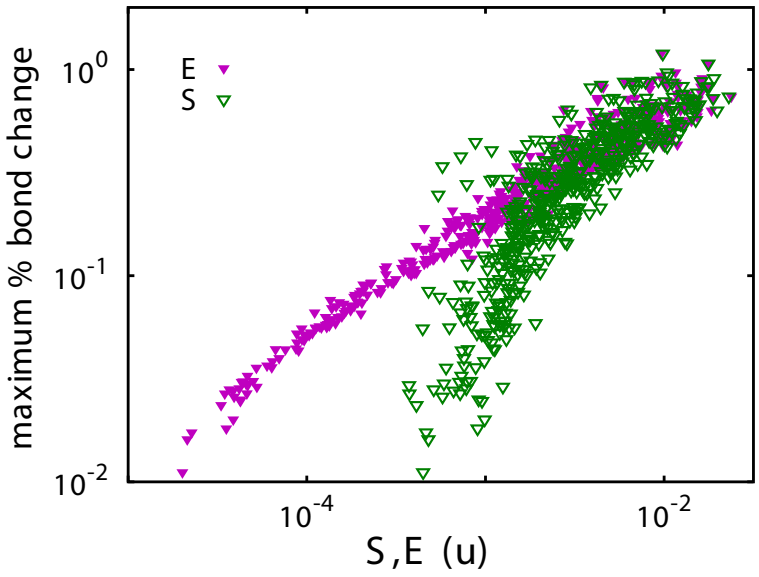

Figure 5.5: The maximum percentage bond change that occurs during an avalanche of stress drop S (open symbols) or energy drop E (closed symbols) in overdamped two-dimensional systems with $L = 109a$. Similar results are obtained for other L and Γ_v.

Changes in bond length are another measure of local deformation that can be used to identify plastic regions. Fig. 5.5 shows the maximum percentage change of any bond in the system as a function of event size. Note that there are almost no events where bonds change less than 2%. These are associated with extremely

small events of order $E \sim 10^{-5}u$. For events in the scaling regime where S and E are comparable ($E > 0.3u$), the largest bond change is at least 20%. This is comparable to the displacements needed to produce a local strain of ϵ_c.

Even the largest events produce only ∼100% bond changes, corresponding to displacements of order a bond length relative to neighbors. This is consistent with the conclusion that larger events produce a uniform amount of dissipation over larger regions rather than larger deformations in a fixed spatial region. The very slow increase in the maximum bond length change with event size for the largest events may be attributed to sampling more bond changes from a fixed distribution. This is consistent with the collapse of the CDF in Fig. 5.5.

5.1.2 Effects of Damping

The damping rate chosen for a simulation can have a dramatic effect on the way plasticity occurs during individual avalanche events. Figure 5.6 shows areas of large vorticity $|\omega| > 0.1$ from quasi-static simulations that illustrate how damping rate influences the plasticity that occurs during an avalanche event. Panel a) illustrates where plasticity occurs during a single event simulated with a damping rate $\Gamma_v t_0 = 0.001$. Below, panel b) shows the plasticity that results from the same initial particle configuration simulated using overdamped dynamics ($\Gamma_v t_0 = 1$). While the initial overdamped event (yellow) is much smaller than the underdamped event, subsequent overdamped events, shown in different colors and symbols, create plasticity

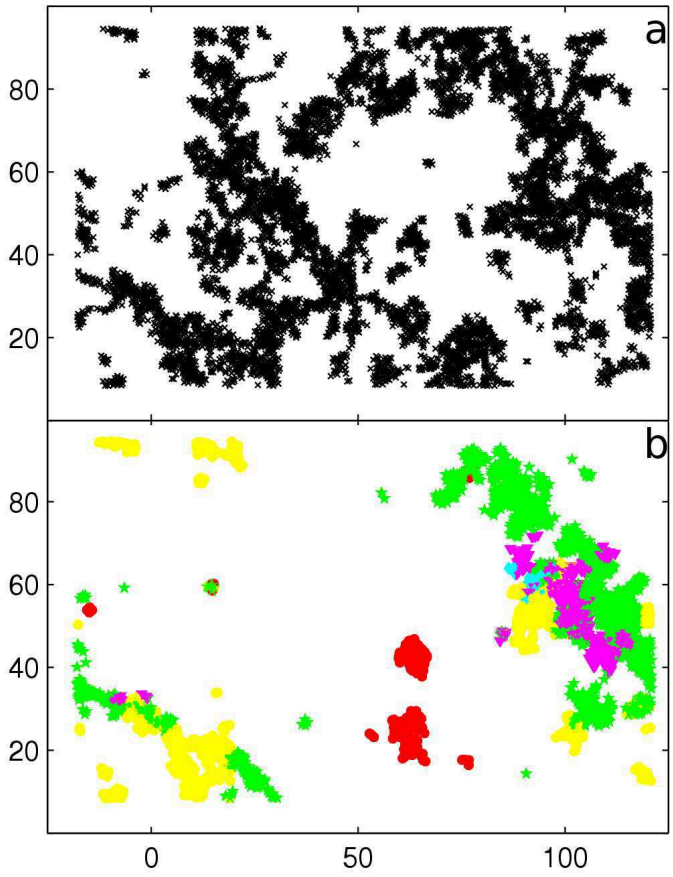

Figure 5.6: The plastic region resulting from avalanches simulated with different Γ_v. (a) The plastic region resulting from a single avalanche at strain ϵ_0 simulated with damping rate $\Gamma_v t_0 = 0.001$ (b) Regions of plasticity ($|\omega| > 0.1$) for five consecutive avalanche events at four different strains with damping $\Gamma_v t_0 = 0.1$ after strain interval $\epsilon - \epsilon_0$: 0% (yellow circle), 0.13% (red circle), 0.18% (green star), 0.6% (cyan triangle) and 0.73% (magenta triangle).

in locations similar to the underdamped event, recreating much of the plasticity from the underdamped event.

It is clear from examination of Fig. 5.6 that not all the areas of plasticity in the underdamped case are deformed during the strain interval shown in the overdamped sequence. The strain interval shown was chosen because at larger strain the overdamped events begin not to coincide with the single underdamped event. This total strain increment of $\Delta\epsilon = 0.0073$ agrees with previous estimates that plastic strain is correlated over a strain interval of $\delta\epsilon = a/L$ (Maloney and Robbins, 2008, 2009). The discrepancy between the underdamped event and the overdamped sequence highlights the fact that over long strain intervals systems simulated with overdamped dynamics sample different energy landscapes because they cannot relax beyond the nearest metastable state.

5.2 Plastic Correlations

The quasi-static strain protocol used above for studying plasticity in individual avalanches restricts the strain interval that can be studied due to both computational and storage limits. As described in Chapter 2 we also implement a constant strain-rate protocol, which is in the quasi-static limit but does not record each individual avalanche event. Our constant rate strain protocol is similar to implementations in previous studies of strained disordered solids (Lemaître and Caroli, 2009; Maloney

and Robbins, 2008). Here the same system is strained at a constant strain rate while the non-affine displacement of each particle is tracked. The non-affine displacement is computed by summing the individual particle displacement at each timestep after subtracting the displacement from the applied strain. The definitions of the local strain measurements are identical to above, with the particle displacement u_i reflecting only the non-affine displacement. We have checked that for our system sizes and strain rates the effective avalanche duration is much less than the inter-avalanche time, placing our simulations firmly in the quasi-static regime found by Lemaître and Caroli (2009).

For the two particular measures below, the diffusive behavior and the long-range correlations, we have compared these measurements with a truly quasi-static simulation protocol, where only the displacements during avalanche events are summed. We have found agreement between the two methods for comparable systems simulated for $L = 875a$ at all damping rates.

5.2.1 Strain Correlations

Figure 5.6 indicates that areas of local plastic deformation can have interesting correlations over large length scales and strain intervals. One way to quantify the correlations in local strain measures is by calculating the power spectrum $S_\epsilon(q) = \langle|\epsilon(q)|^2\rangle$. The quantity $\epsilon(q)$ is the Fourier transform of a local, position dependent strain measurement. Results from the strain quantities ϵ_d and ω are of interest, as is

the volumetric strain ϵ_I. This quantity is defined in the normal way as the trace of the strain tensor divided by the dimension d, or $\epsilon_I = 1/2(\epsilon_{xx}+\epsilon_{yy})$ in two dimensions. The power-spectrum of the vorticity ω has previously been shown to display long-range correlations with an angular dependence (Maloney and Robbins, 2009). An important question is whether other strain measures display the same features.

As in previous sections, results for $S(q)$ come from the steady-state regime. The results shown in this section are for systems with constant shear rate. Results are independent of shear rate in the quasi-static regime. The quasi-static regime corresponds to strain rates $\dot{\epsilon} = 10^{-6}$ for $\Gamma_v t_0 = 0.001$ and 0.1 and $\dot{\epsilon} = 2\text{x}10^{-7}$ for $\Gamma_v t_0 = 1$.

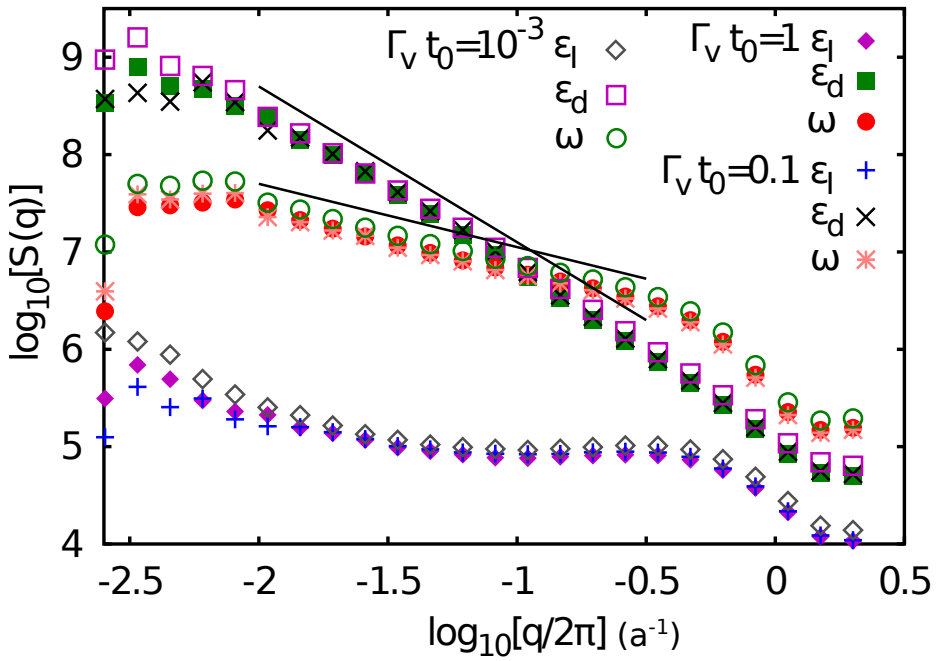

Figure 5.7: The power spectrum $S(q)$ for three different local strain measures, the dilational strain ϵ_I (diamonds and +), deviatoric strain ϵ_d (squares and x), and the displacement vorticity ω (circles and *). Both ϵ_d and ω show long-range correlations while ϵ_I does not.

Figure 5.7 shows $S(q)$ calculated for the strain measures ϵ_d, ϵ_I, and ω for the $L = 875a$ system. The function $\log_{10}(S(q))$ has been averaged over all angles. Filled symbols represent viscous damping $\Gamma_v t_0 = 1$, open symbols $\Gamma_v t_0 = 0.1$, and crossmarks represent $\Gamma_v t_0 = 0.001$. Data for the three different strain measures vary greatly. The dilational strain has a generally low value over almost the entire range of q. The vorticity follows a power-law with slope 0.6, indicating long-range correlations. The power spectrum for the deviatoric strain displays a steeper slope of ~ 2. The open, closed, and crossmark symbols all fall roughly atop one another for each of the three different strain measures, indicating that damping rate Γ has relatively little effect on the correlations in these measures. Note that this is only because particle displacements are calculated over a strain interval much larger than the separation between avalanches. The open symbols are slightly higher than the other symbols, indicating that the low damping regime shows slightly larger magnitudes over all q.

When calculating $S(q)$ in a finite system, it is important to distinguish features that are independent of system size from those which are influenced by the finite sample size. Figure 5.8 shows $S(q)$ for the three local strain quantities for system sizes $L = 875a$, $438a$, and $109a$. As with the finite-size scaling performed in Chapter 3 one can use different system sizes to see how deviations from a master curve occur with system size. In Fig. 5.8a) and b) we see that the power-law behavior in $S(q)$ persists to smaller wavevector or larger length scales with increasing system size, with a consistent slope. For the vorticity in Fig. 5.8a) the slope is between 0.6 and 0.7 for

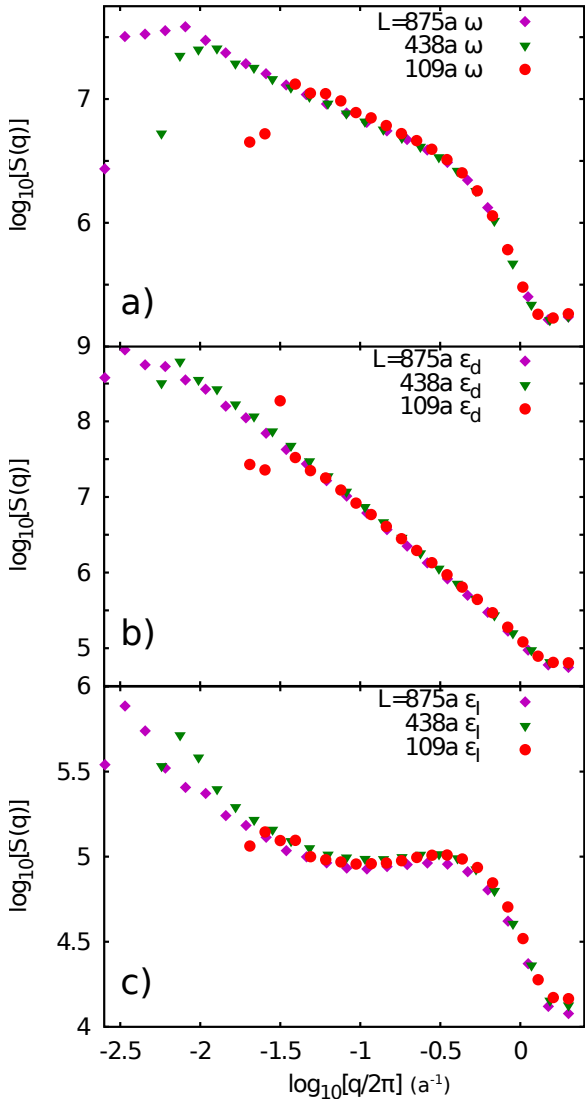

Figure 5.8: Power spectrum $S(q)$ of different strain measures a) ω, b) ϵ_d, and c) ϵ_I. For each quantity the angle-averaged log power-spectrum has been computed for system sizes $L = 109a$, $438a$, and $875a$. For both ω and ϵ_d consistent power-law behavior is seen for all system sizes, with the range of the power law extending to smaller q (larger length scales) as system size increases. The dilational strain shows much weaker correlations.

all L. The deviatoric strain ϵ_d has a steeper slope in Fig. 5.8b) of ~ 1.75.

The long-range correlations displayed by ϵ_d and ω contrast with the lack of structure in ϵ_I. Both ϵ_d and ω measure deformations associated with shear, suggesting that this commonality is the source of the long-range correlations. The formation of long-range structure in shear components of the strain field is consistent with the loading and unloading of the system in both elemental and large scale shear events (Falk and Langer, 1998; Maloney and Robbins, 2009; Talamali et al., 2011).

We would also like to test whether all quantities related to shear strain display the anisotropy found previously (Maloney and Robbins, 2009). Figure 5.9 compares the power spectrum $S(q)$ for the deviatoric strain ϵ_d and displacement vorticity ω along different angles θ in reciprocal space. Angles of $\theta = 0, \pi/8$, and $\pi/4$ with respect to the direction of extension are shown. For both ϵ_d and ω the power spectrum $S(q)$ has four-fold symmetry, with $n\pi/4$ for odd n showing the steepest slope. Figure 5.9a) shows the power spectrum of the deviatoric strain, while Fig. 5.9b) shows the power spectrum for the vorticity. There is a remarkable difference in the two quantities, with the vorticity showing stronger angular dependence. As reported previously (Maloney and Robbins, 2009), the slope of the power-law region changes from ~ 0.1 to ~ 1.2 between the angles from $\theta = 0$ to $\pi/4$. The deviatoric strain shows a much weaker dependence on angle.

The discrepancy between the deviatoric strain and the vorticity is striking. As noted by previously, (Maloney and Robbins, 2009) the vorticity has the interesting

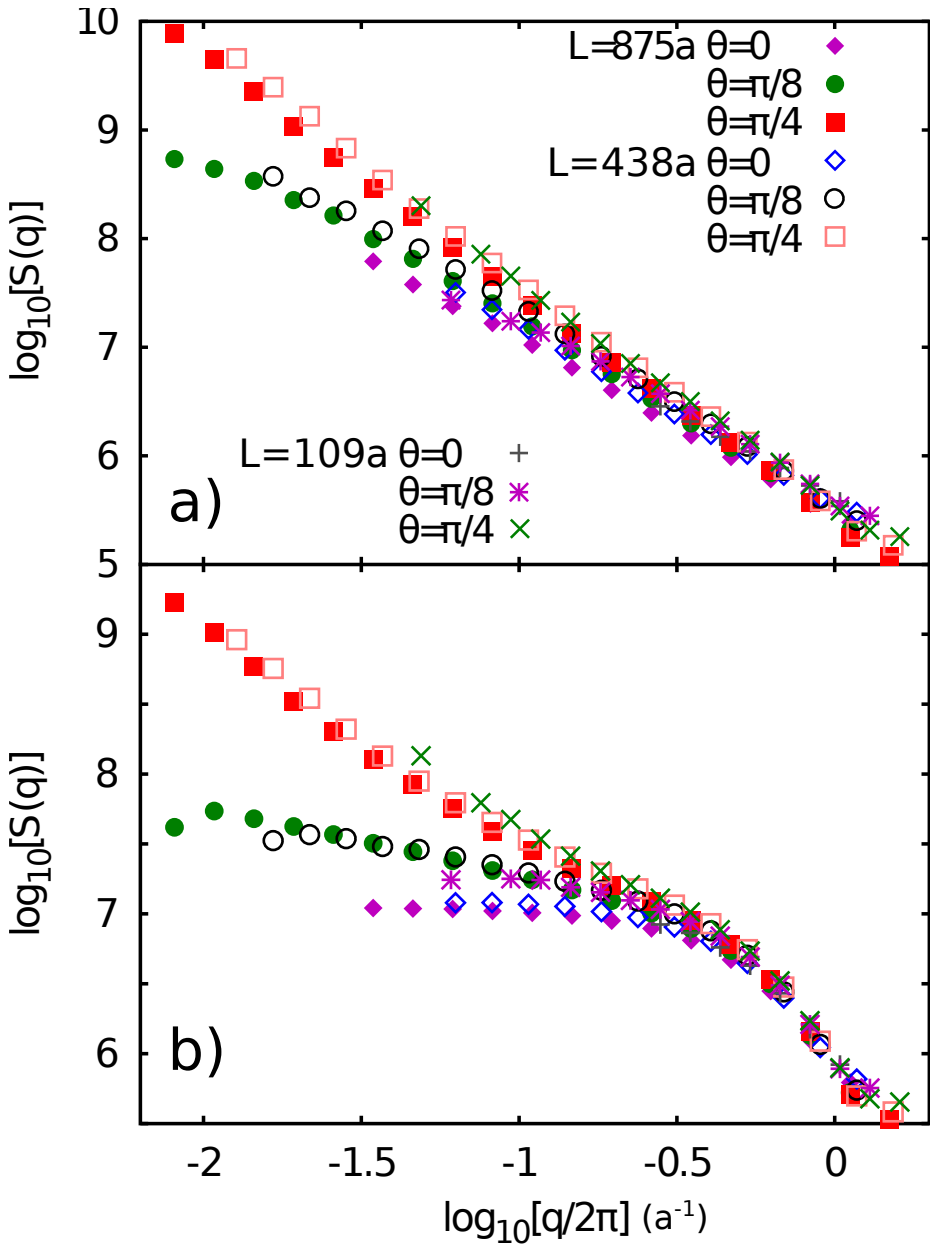

Figure 5.9: The power spectrum $S(q)$ for a) the deviatoric strain ϵ_d and b) the vorticity of the displacement field ω. Both quantities are shown at angles $\theta = 0$ (diamonds and +),$\theta = \pi/8$ (circles and *), and $\theta = \pi/4$ (squares and x). Different symbol types represent system size $L = 875a$, (filled) $438a$ (open), and $109a$ (crossmarks). The contrast in angular dependence is striking, with the vorticity showing strong angular dependence and the deviatoric strain showing only slight angular dependence.

characteristic that it is sensitive to both the magnitude and sense of strain. In contrast with quantities like ϵ_d that derive from a symmetrized strain tensor, the vorticity is maximized for local rotations and changes sign between clockwise and counter-clockwise rotations. The power-spectrum of the absolute value of the vorticity $|\omega|$ was constructed to test of the importance of rotation in the angular dependence of the long-range correlations. This quantity shows a very weak angular dependence and is similar to the power spectrum of ϵ_d. This confirms the conjecture that the sense of the shear strain may be important in the angular dependence of long-range correlations in sheared disordered solids. The interesting behavior of the vorticity highlights the potential drawbacks of using invariants and symmetrized forms to describe properties of an underlying displacement field.

One may also wonder if the angular dependence seen in the vorticity and the deviatoric strain are independent of damping rate. Given the result in Fig. 5.7, it is difficult to imagine that the angular dependence shows significant damping-rate dependence. Figure 5.10 compares the deviatoric strain and vorticity for different angles and damping rates. The curves appear to have a shift downward in magnitude with increasing damping rate, but the angular dependence seems to be independent of damping rate.

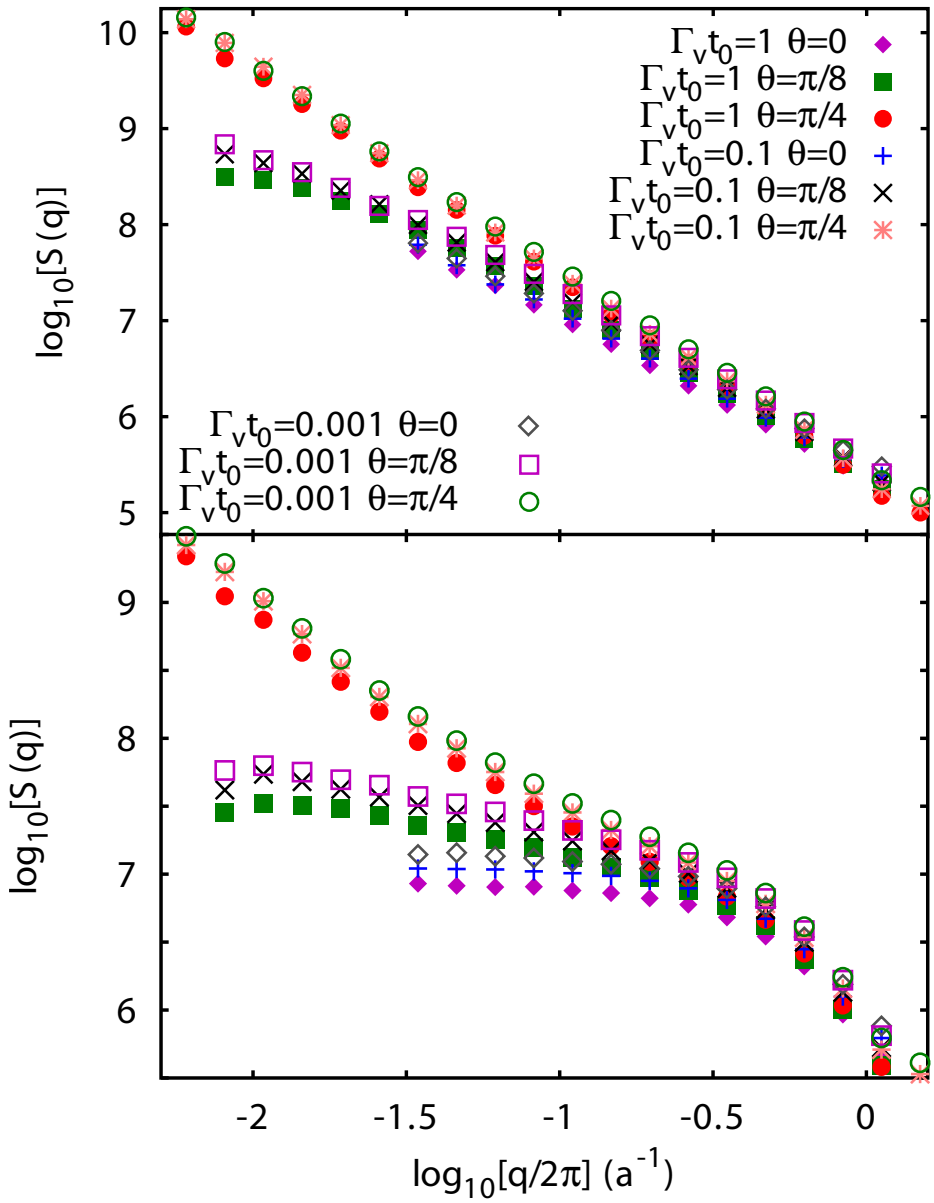

Figure 5.10: The power spectrum $S(q)$ for a) the deviatoric strain ϵ_d and b) the vorticity of the displacement field ω. Both quantities are shown at angles $\theta = 0$ (diamonds and +),$\theta = \pi/8$ (circles and *), and $\theta = \pi/4$ (squares and x). Different symbol types represent damping rate $\Gamma_v t_0 = 1$, $\Gamma_v t_0 = 0.1$, and $\Gamma_v t_0 = 0.001$. All data is from system size $L = 875a$. The data are approximately independent of damping. There are slight shifts to lower magnitudes for increased damping, but the angular dependence in both measures is independent of damping.

5.2.2 Diffusion

One of the most basic measures of particle displacements is the mean-square displacement, related to particle diffusion over time in fluids. By averaging the individual particle displacements we can calculate the mean-square non-affine displacement

$$\langle \Delta r^2 \rangle(t) \equiv \langle |\vec{r}(t) - \vec{r}(0)|^2 \rangle \tag{5.5}$$

over strain intervals. In the past this quantity was found to be linear in the applied strain for both overdamped and inertial systems (Lemaître and Caroli, 2007, 2009; Maloney and Robbins, 2008). The prefactor of the linear relations can be identified as an effective diffusion constant $D(L)$:

$$\langle \Delta r^2 \rangle(t) = D(L)\Delta\gamma. \tag{5.6}$$

In contrast to equilibrium diffusion where D is independent of size, D increases with system size.

Figure 5.11 shows the system size dependent diffusive behavior. Data for system sizes $L = 875a, 438a$ and $109a$ rise with increasing system size. The slope of the line on log-log axes is unity indicating diffusive behavior after an initial strain interval. For each system size results from the three different damping rates overlap, indicating that the particle diffusion is equivalent for the different damping cases.

The L dependence of the diffusion constant is tested in Figs. 5.12 a) and b), where the strain has been multiplied by system size. The collapse of the data for all the systems simulated shows that the diffusion constant D is proportional to

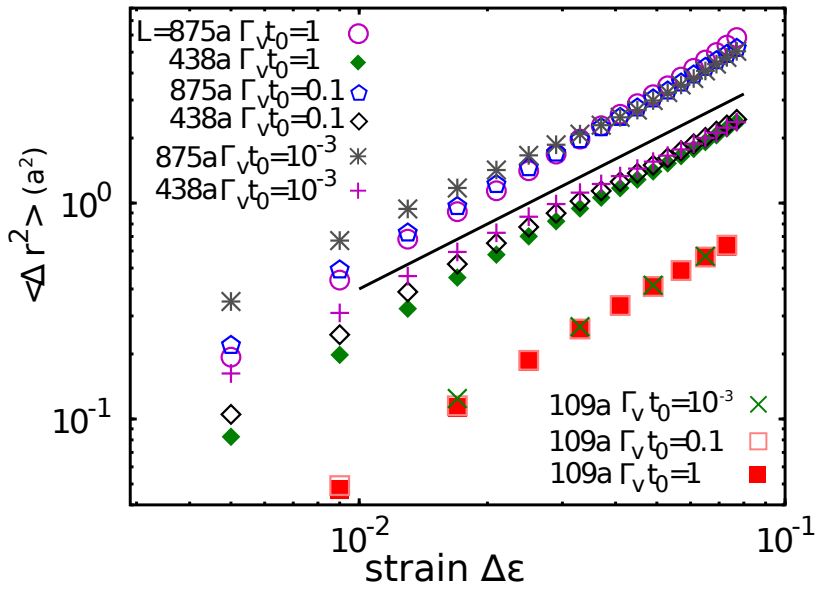

Figure 5.11: Mean-square displacement $\langle \Delta r^2 \rangle$ as a function of strain interval. Results for different damping rates Γ_v are indistinguishable after an initial strain interval. Different system sizes $L = 875a, 438a$ and $109a$ are spaced approximately as L.

L, independent of damping rate. This result has been found previously, but the explanation of Lemaître and Caroli (2009) is not consistent with the overlap of results for different damping rates.

Lemaître and Caroli (2009) argued previously that the diffusion was due to linear faults created by individual avalanches of maximum size proportional to L. This essentially assumes the exponent $\alpha = 1$, which is only approximately true for the crossover and overdamped systems and Fig. 5.6 illustrates that individual avalanches are hardly linear faults. Furthermore, the exponent $\alpha = 1.6$ in the underdamped limit, yet even for this damping the diffusion constant is proportional to L.

Figure 5.13 shows a finite-difference of the mean-square displacement curves shown in Fig. 5.11. The finite difference is taken over a strain interval $\delta\epsilon$. The data have

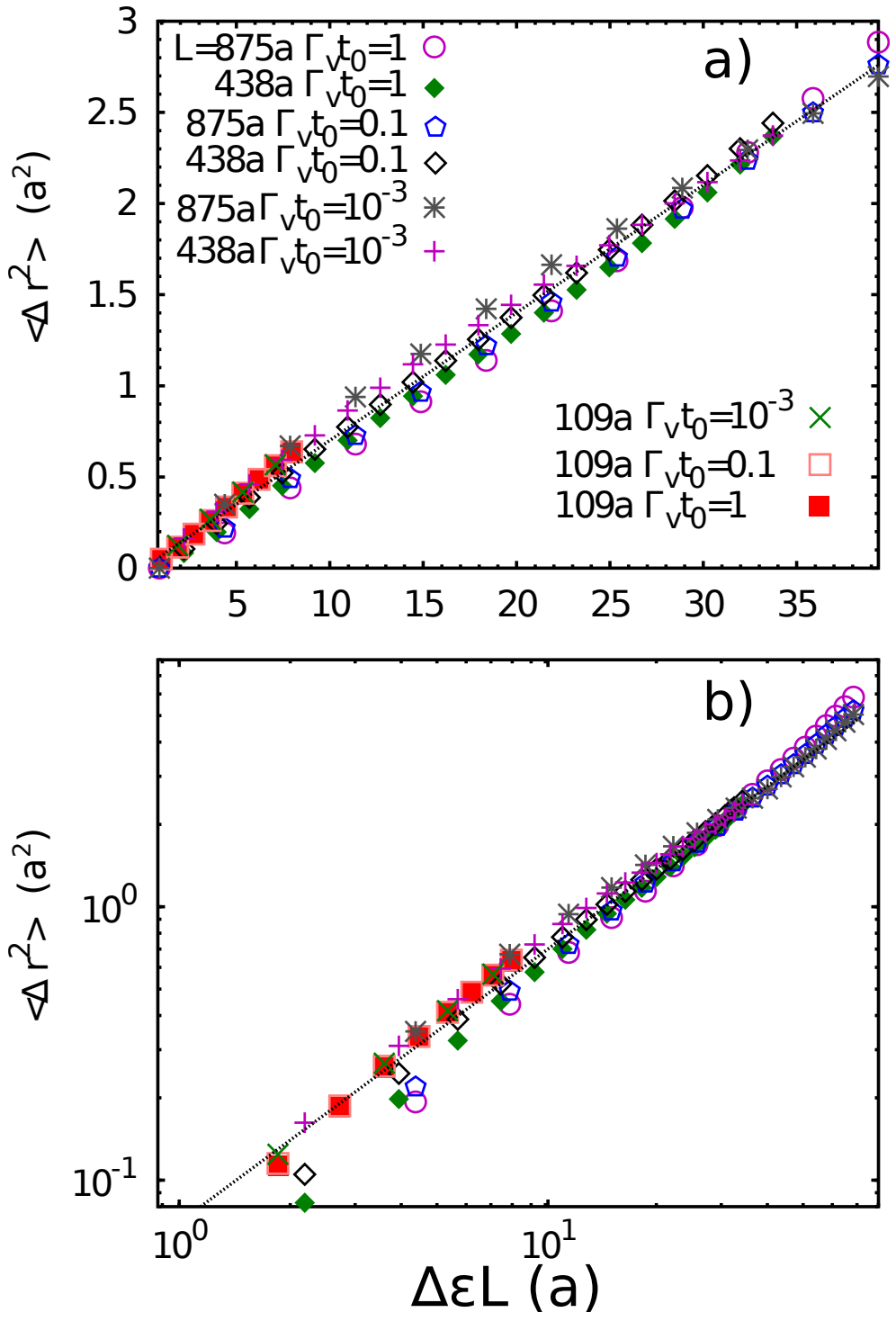

Figure 5.12: Mean-square displacement $\langle \Delta r^2 \rangle$ as a function of scaled strain interval. Strain is scaled by system size L, indicating that the effective diffusion constant is proportional to L. This collapse is good for both a) linear and b) log-log scales. The line drawn in each figure reflects $D/L = 0.07$, an estimate of the prefactor of the system-size dependent diffusion constant.

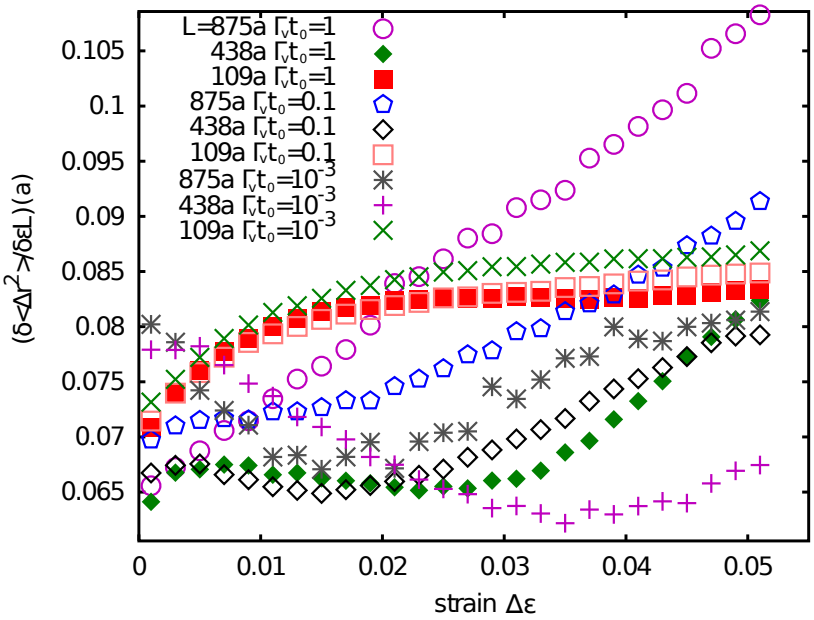

Figure 5.13: Finite difference of the mean-square displacement as a function of strain.

been scaled by system size L to show the effective diffusion constant D/L for different parameters as a function of strain. Note that the $L = 875a$ system at damping $\Gamma_v t_0 = 1$ is strained at a lower strain rate, limiting the collection of statistics to only about four independent realizations for this set of parameters. It is clear that there are significant fluctuations due to poor statistics Statistical errors are on the order 5% for $L = 109a$ ranging up to $\sim 30\%$ for $L = 875a$. Still, there seems to be a clear system size dependence, with a value of $D/L \approx 0.08a$.

The value $D/L \approx a/12$ was given by Maloney and Robbins (2008) based on a geometrical argument and observation of through-going slip lines at strain intervals of a/L. These slip lines create an average mean-squared displacement of $a^2/12$, based on a zone of finite-width accommodating nearly the entire displacement with a high

local strain. Because the slip lines occur at regular a/L strain intervals, larger systems produce faults more frequently and experience higher diffusion.

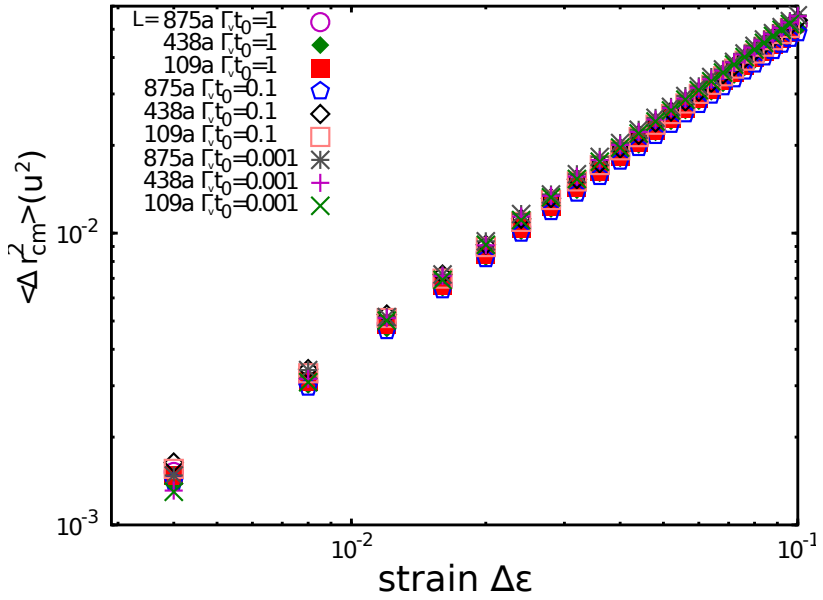

Figure 5.14: Mean-square displacement from the neighborhood center-of-mass as a function of strain interval. Results for different damping rates Γ_v and system size L are indistinguishable.

In order to investigate the origin of the system-size dependent diffusion seen in Figs. 5.11, 5.12 a) and b) as well as by other groups, we also calculate each particle's diffusive motion relative to its local neighborhood. We define the center of mass as the sum of the positions of the N_{nn} neighbors of a particle $\vec{r}_{cm} = 1/N_{nn} \sum_j \vec{r}_j$. We use this position to calculate each particle's mean-square displacement relative to the neighbors' center of mass

$$\langle \Delta r_{cm}^2 \rangle(t) \equiv < |(\vec{r}(t) - \vec{r}_{cm}(t)) - (\vec{r}(0) - \vec{r}_{cm}(0))|^2 > . \tag{5.7}$$

Figure 5.14 shows particle diffusion relative to the center-of-mass of its neighbor

particles. Unlike the raw particle diffusion curves, results from different system sizes collapse with no scaling, indicating that this relative diffusion is independent of system size. Like the particle diffusion, this quantity is also independent of damping rate. The system-size independence of the center-of-mass diffusion is consistent with spatial correlations in displacements leading to the system-size dependent diffusive behavior.

Diffusive behavior observed in three dimensions is different from the behavior observed in two dimensions. Figure 5.15 shows the effective diffusion associated with the non-affine particle displacement in three dimensions on both log-log and linear axes. The contrast with the two-dimensional behavior is apparent. System sizes $L = 20a$ to $80a$ are shown and within this range the non-affine mean-square displacement of the particles shows no system-size dependence. The data for the different system sizes collapse on a single curve on the log-log scales in Fig. 5.15b). The data show more variation on the linear scales in Fig. 5.15a), yet show only $\sim$10% difference over a factor of four in system length and a factor of 64 in particle number. Statistical uncertainties are comparable to these differences. Note that diffusion relative to the neighborhood center-of-mass is approximately the same in 3D.

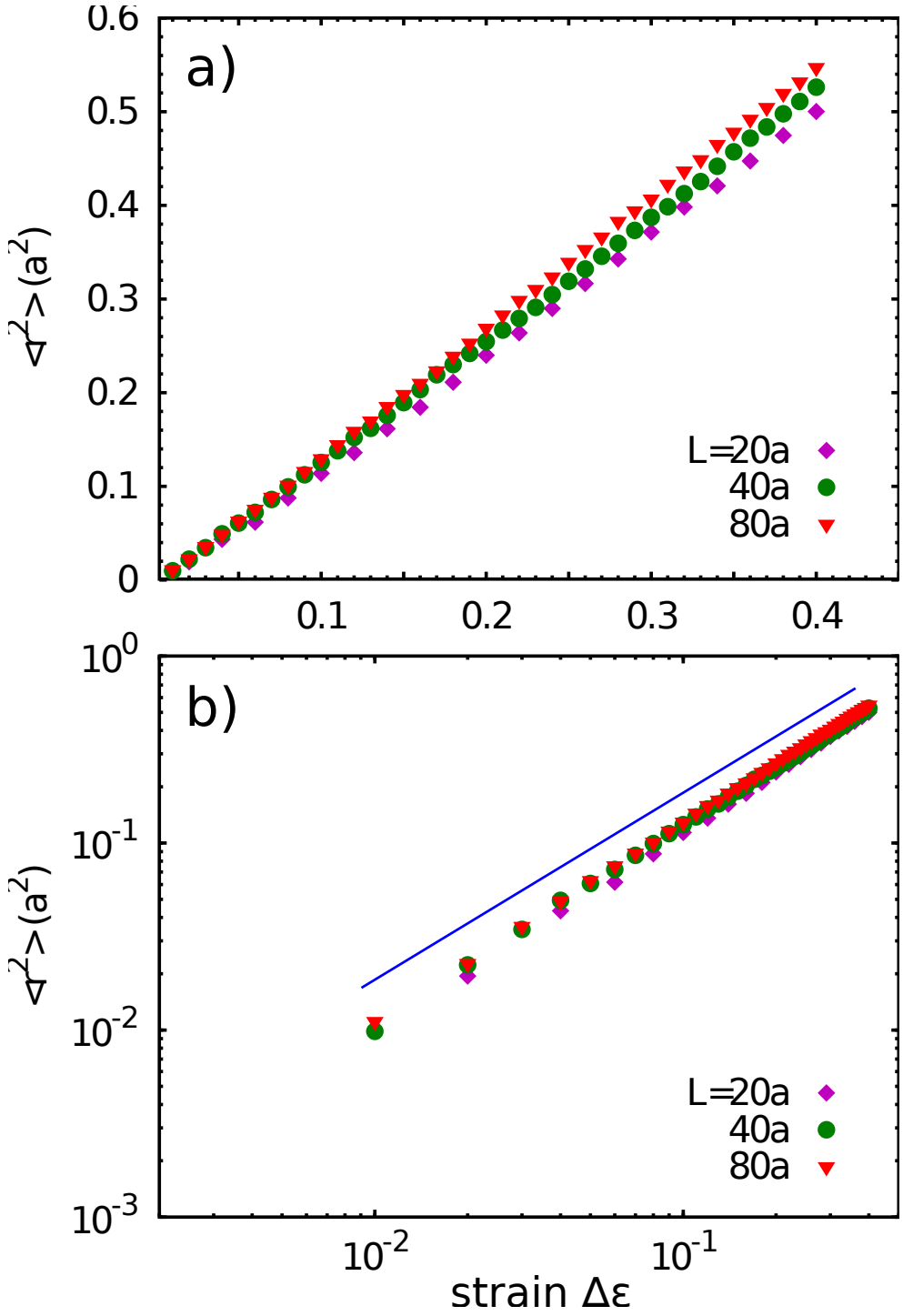

Figure 5.15: Mean-square displacement $\langle \Delta r^2 \rangle$ as a function of strain interval in three dimensions. The effective diffusion constant is independent of L. This leads to a collapse both a) linear and b) log-log scales without rescaling the data. The slope of the line drawn in b) is one indicating diffusive behavior.

Chapter 6

Conclusion

In this thesis molecular dynamics simulations have been used to explore the role of inertia in the deformation of disordered solids. Contrary to previous results and predictions, inertia does not destroy critical behavior but instead leads to new classes of critical behavior. Three classes of behavior are found in three distinct damping regimes, the limiting case of overdamped dynamics, the limit of underdamped dynamics, and a crossover regime between the two.

Quasi-static simulations are used to study the properties of the scale invariant avalanches found in each of the three damping regimes. These avalanches are the hallmark of a second-order phase transition. Stress and energy drops are studied and their rate-distributions are used to measure critical exponents. Critical exponents are found in each of the three damping regimes, with their values indicating the different universality classes. The relationship between stress and energy drop is explored,

as well as the connection between critical scaling exponents and the steady state distribution of stress values.

In Chapter 4 a comparison is made between two different dissipative mechanisms. The Galilean-invariant and viscous damping mechanisms display equivalent behavior in the overdamped and underdamped limits. In contrast, the crossover between the two limiting cases occurs differently for the two damping mechanisms. For the viscous damping the scaling exponent α remains close to its overdamped value while for the Galilean-invariant dissipation the value is closer to the value in the underdamped limit. The behavior of the exponent α as it changes from one limiting case to the other motivates a closer study of the crossover behavior between the damping limits for the two different dissipative mechanisms. The system-size dependent collapse of the data in the viscous (Galilean-invariant) underdamped (overdamped) limit may be explained by a simple timescale argument. Such a size dependence may also indicate that systems with intrinsic viscous (Galilean-invariant) damping will tend not to be found in the underdamped (overdamped) limits in the thermodynamic limit.

Plastic deformation in sheared disordered solids is quantified in Chapter 5. A definition of plastic deformation is formulated based on invariants of the strain tensor. Based on this definition, the extent of plastic deformation in an avalanche event is found to be proportional to the energy dissipated over a wide range of energies. Correlations in the spatial dependence of local strain field are studied via the power spectrum $S(q)$ of the symmetric and deviatoric strain invariants as well as through the

vorticity of the displacement field ω, which is sensitive to local rotations. Interesting and distinct behavior is found in the three quantities: The deviatoric strain is found to have power-law correlations over a wide range of length scales. These correlations show only weak angular dependence. In contrast, the vorticity displays long-range correlations with a strong angular dependence. Finally, the strain invariant associated with dilational strains displays no long-range correlations. These results are found to be independent of damping rate.

Another property measured is the diffusive behavior in the non-affine particle displacements. The effective diffusion constant is found to be system size dependent in two dimensions independent of damping rate. The effective diffusion constant is proportional to the system size, independent of damping rate. This finding validates some previous work (Maloney and Robbins, 2008), but contradicts another explanation of this diffusive phenomenon (Lemaître and Caroli, 2009). The system size-dependent diffusive behavior in two dimensions contrasts with the picture in three dimensions, where the effective diffusion constant is independent of system size.

Some questions have been raised by the research and results presented. To the question of how exactly inertia influences the growth of avalanches from a single instability up to larger scales there is no simple answer. In fact, results showing that inertia changes how the system samples the potential energy landscape imply a nonlinearity that is difficult to address. How can one isolate the effect of inertia on an avalanche event when the state of the system depends on the system history? This

also appears to frustrate attempts to add inertial effects to simplified models. One way to address this issue might be through analysis of differences in states sampled with different damping rates. Finding which microscopic details influence the trajectories shown in Fig. 3.1 appears very difficult, however.

A more immediately addressable question is related to the discrepancies between two and three-dimensional diffusion. The lack of system-size dependence in three dimensions raises interesting questions. The L dependence of the two-dimensional diffusion seems not directly linked to avalanche behavior in the quasi-static limit. Geometry appears to play a key role, with particle displacements in three dimensions accommodated without a large number of highly-correlated particle displacements. This suggests a link between the quantity $S(q)$ and the diffusive behavior. Simulations and measurements of the strain correlations in three dimensions could provide some information about why the difference in diffusive behavior exists.

Bibliography

M. J. Alava, P. K. V. V. Nukala, and S. Zapperi. *Advances in Physics*, 55(3-4): 349–476, May 2006.

A. S. Argon. *Acta Metallurgica*, 27(1):47–58, Jan 1979.

N. Bailey, J. Schiøtz, and K. Jacobsen. *Phys. Rev. B*, 69(14):1–11, Apr 2004.

N. P. Bailey, J. Schiøtz, A. Lemaître, and K. W. Jacobsen. *Phys. Rev. Lett.*, 98: 095501, Feb 2007.

S. Besson, G. Debrégeas, S. Cohen-Addad, and R. Höhler. *Phys. Rev. Lett.*, 101: 214504, Nov 2008.

D. Bi, J. Zhang, B. Chakraborty, and R. P. Behringer. *Nature*, 480(7377):355–8, Dec 2011.

N. V. Brilliantov, F. Spahn, J. Hertzsch, and T. Pöschel. *Phys. Rev. E*, 53:5382–5392, May 1996.

R. Burridge and L. Knopoff. *Bulletin of the Seismological Society of America*, 57(3): 341–371, 1967.

J. M. Carlson. *Phys. Rev. A*, 44:6226–6232, Nov 1991.

BIBLIOGRAPHY

J. M. Carlson and J. S. Langer. *Phys. Rev. Lett.*, 62:2632–2635, May 1989.

J. M. Carlson, J. S. Langer, B. E. Shaw, and C. Tang. *Phys. Rev. A*, 44:884–897, Jul 1991.

K. Chen, M. L. Manning, P. J. Yunker, W. G. Ellenbroek, Z. Zhang, A. J. Liu, and A. G. Yodh. *Phys. Rev. Lett.*, 107:108301, Aug 2011.

A. H. Clark, L. Kondic, and R. P. Behringer. *Phys. Rev. Lett.*, 109:238302, Dec 2012.

S. Cohen-Addad, R. Höhler, and Y. Khidas. *Phys. Rev. Lett.*, 93:028302, Jul 2004.

K. Dahmen and J. P. Sethna. *Phys. Rev. B*, 53:14872–14905, Jun 1996.

K. Dahmen, Y. Ben-Zion, and J. T. Uhl. *Nature Physics*, 7(7):554–557, Mar 2011.

Karin A. Dahmen, Yehuda Ben-Zion, and Jonathan T. Uhl. *Phys. Rev. Lett.*, 102: 175501, Apr 2009.

M. J. Demkowicz and A. S. Argon. *Phys. Rev. Lett.*, 93:025505, Jul 2004.

M. J. Demkowicz and A. S. Argon. *Phys. Rev. B*, 72:245206, Dec 2005.

M. Dennin and C. M. Knobler. *Phys. Rev. Lett.*, 78:2485–2488, Mar 1997.

D. J. Durian. *Phys. Rev. E*, 55:1739–1751, Feb 1997.

J. D. Eshelby. *Proceedings of the Royal Society of London. Series A. Mathematical and Physical Sciences*, 241(1226):376–396, 1957.

M. L. Falk and J. S. Langer. *Phys. Rev. E*, 57:7192–7205, Jun 1998.

M. L. Falk, J. S. Langer, and L. Pechenik. *Phys. Rev. E*, 70:011507, Jul 2004.

D. S. Fisher. *Physics reports*, 301:113–150, 1998.

Daniel S. Fisher. *Phys. Rev. B*, 31:1396–1427, Feb 1985.

BIBLIOGRAPHY

N. Friedman, A. T. Jennings, G. Tsekenis, Ju-Young Kim, M. Tao, J. T. Uhl, J. R. Greer, and K. A. Dahmen. *Phys. Rev. Lett.*, 109:095507, Aug 2012.

N. W. Hayman, L. Ducloué, K. L. Foco, and K. E. Daniels. *Pure and Applied Geophysics*, 168(12):2239–2257, Feb 2011.

G. A. Held, D. H. Solina, H. Solina, D. T. Keane, W. J. Haag, P. M. Horn, and G. Grinstein. *Phys. Rev. Lett.*, 65:1120–1123, Aug 1990.

M. Herrera, S. McCarthy, S. Slotterback, E. Cephas, W. Losert, and M. Girvan. *Phys. Rev. E*, 83:061303, Jun 2011.

P. J. Hoogerbrugge and J. M. V. A. Koelman. *EPL (Europhysics Letters)*, 19(3):155, 1992.

H. M. Jaeger, C. Liu, and S. R. Nagel. *Phys. Rev. Lett.*, 62:40–43, Jan 1989.

D. Jang and J. R Greer. *Nature materials*, 9(3):215–219, 2010.

D. Jang, C. T. Gross, and J. R. Greer. *International Journal of Plasticity*, 27(6):858 – 867, 2011.

S. Karmakar, A. Lemaître, E. Lerner, and I. Procaccia. *Phys. Rev. Lett.*, 104:215502, May 2010.

L. Kondic, X. Fang, W. Losert, C. S. O'Hern, and R. P. Behringer. *Phys. Rev. E*, 85: 011305, Jan 2012.

J. S. Langer. *Phys. Rev. E*, 85:051507, May 2012.

A. Lemaître and C. Caroli. *Phys. Rev. E*, 76:036104, Sep 2007.

A. Lemaître and C. Caroli. *Phys. Rev. Lett.*, 103:065501, Aug 2009.

BIBLIOGRAPHY

A. Lemaître and C. Maloney. *Journal of Statistical Physics*, 123(2):415–453, Apr 2006.

E. Lerner and I. Procaccia. *Phys. Rev. E*, 79:066109, Jun 2009.

R. Maimon and J. M. Schwarz. *Phys. Rev. Lett.*, 92:255502, Jun 2004.

C. Maloney and A. Lemaître. *Phys. Rev. Lett.*, 93:195501, Nov 2004a.

C. Maloney and A. Lemaître. *Phys. Rev. Lett.*, 93:016001, Jul 2004b.

C. Maloney and M. Robbins. *Phys. Rev. Lett.*, 102(22):225502, Jun 2009.

C. E. Maloney. *Phys. Rev. Lett.*, 97:035503, Jul 2006.

C. E. Maloney and A. Lemaître. *Phys. Rev. E*, 74:016118, Jul 2006.

C. E. Maloney and M. O. Robbins. *Journal of Physics: Condensed Matter*, 20(24): 244128, Jun 2008.

M. L. Manning and A. J. Liu. *Phys. Rev. Lett.*, 107:108302, Aug 2011.

M. L. Manning, E. G. Daub, J. S. Langer, and J. M. Carlson. *Phys. Rev. E*, 79: 016110, Jan 2009.

M. C. Marchetti. *Pramana*, 64(6):1097–1107, Jun 2005.

N. Martys, M. Cieplak, and M. O. Robbins. *Phys. Rev. Lett.*, 66:1058–1061, Feb 1991a.

N. Martys, M. O. Robbins, and M. Cieplak. *Phys. Rev. B*, 44:12294–12306, Dec 1991b.

M. C. Miguel, A. Vespignani, S. Zapperi, J. Weiss, and J. R. Grasso. *Nature*, 410 (6829):667–71, Apr 2001.

BIBLIOGRAPHY

B. Miller, C. O'Hern, and R. P. Behringer. *Phys. Rev. Lett.*, 77:3110–3113, Oct 1996.

C. R. Myers and J. P. Sethna. *Phys. Rev. B*, 47:11171–11193, May 1993.

O. Narayan and D. S. Fisher. *Phys. Rev. Lett.*, 68:3615–3618, Jun 1992.

K. N. Nordstrom, E. Verneuil, P. E. Arratia, A. Basu, Z. Zhang, A. G. Yodh, J. P. Gollub, and D. J. Durian. *Phys. Rev. Lett.*, 105:175701, Oct 2010.

I. K. Ono, S. Tewari, S. A. Langer, and A. J. Liu. *Phys. Rev. E*, 67:061503, Jun 2003.

Ferenc Pázmándi, Richard T. Scalettar, and Gergely T. Zimányi. *Phys. Rev. Lett.*, 79:5130–5133, Dec 1997.

O. Perković, K. A. Dahmen, and J. P. Sethna. *Phys. Rev. B*, 59:6106–6119, Mar 1999.

G. Picard, A. Ajdari, F. Lequeux, and L. Bocquet. *The European physical journal. E, Soft matter*, 15(4):371–81, Dec 2004.

S. Plimpton. *Journal of Computational Physics*, 117(1):1–19, Mar 1995.

C. P. C. Prado and Z. Olami. *Phys. Rev. A*, 45:665–669, Jan 1992.

V. Privman. *Finite Size Scaling and Numerical Simulation of Statistical Systems*. World Scientific Publishing Company, Incorporated, 1990.

P. Schall, D. A. Weitz, and F. Spaepen. *Science (New York, N.Y.)*, 318(5858):1895–9, Dec 2007.

C. H. Scholz. *The mechanics of earthquakes and faulting*. Cambridge University Press, 2002.

J. M. Schwarz and D. S. Fisher. *Phys. Rev. Lett.*, 87:096107, Aug 2001.

J. M. Schwarz and D. S. Fisher. *Phys. Rev. E*, 67:021603, Feb 2003.

BIBLIOGRAPHY

A. Shekhawat, S. Zapperi, and J. P. Sethna. *Phys. Rev. Lett.*, 110:185505, Apr 2013.

L. E. Silbert, D. Ertaş, G. S. Grest, T. C. Halsey, D. Levine, and S. J. Plimpton. *Phys. Rev. E*, 64:051302, Oct 2001.

L. E. Silbert, A. J. Liu, and S. R. Nagel. *Phys. Rev. E*, 79:021308, Feb 2009.

S. Slotterback, M. Mailman, K. Ronaszegi, M. van Hecke, M. Girvan, and W. Losert. *Phys. Rev. E*, 85:021309, Feb 2012.

D. Sornette. *Journal of Physics A: Mathematical and General*, 22:L243, 1989.

F. Spaepen. *Acta Metallurgica*, 25(4):407–415, 1977.

D. Stauffer and A. Aharony. *Introduction To Percolation Theory*. Taylor & Francis, 1994.

B. A. Sun, H. B. Yu, W. Jiao, H. Y. Bai, D. Q. Zhao, and W. H. Wang. *Phys. Rev. Lett.*, 105:035501, Jul 2010.

B.A. Sun, S. Pauly, J. Tan, M. Stoica, W.H. Wang, U. Kühn, and J. Eckert. *Acta Materialia*, 60(10):4160 – 4171, 2012.

M. Talamali, V. Petäjä, D. Vandembroucq, and S. Roux. *Phys. Rev. E*, 84:016115, Jul 2011.

A. Tanguy, F. Leonforte, and J-L. Barrat. *The European physical journal. E, Soft matter*, 20(3):355–64, Jul 2006.

S. Tewari, D. Schiemann, D. J. Durian, C. M. Knobler, S. A. Langer, and A. J. Liu. *Phys. Rev. E*, 60:4385–4396, Oct 1999.

M. Tsamados, A. Tanguy, C. Goldenberg, and Jean-Louis Barrat. *Phys. Rev. E*, 80:

026112, Aug 2009.

B. Utter and R. P. Behringer. *Phys. Rev. E*, 69:031308, Mar 2004.

B. Utter and R. P. Behringer. *Phys. Rev. Lett.*, 100:208302, May 2008.

F.F. Wu, Z.F. Zhang, J. Shen, and S.X. Mao. *Acta Materialia*, 56(4):894 – 904, 2008.

L.-Q. Xing, Y. Li, K. T. Ramesh, J. Li, and T. C. Hufnagel. *Phys. Rev. B*, 64:180201, Oct 2001.

M. Zaiser. *Advances in Physics*, 55(1-2):185–245, 2006.

S. Zapperi, A. Vespignani, and H. E. Stanley. *Nature*, 388(6643):658–659, 1997.

H. P. Zhang and H. A. Makse. *Phys. Rev. E*, 72:011301, Jul 2005.

Vita

K. Michael Salerno received his A.B. degree in political science from Princeton University in 2004. He worked with Teach For America in Houston, Texas for two years before continuing his studies in physics at the College of William and Mary. He began his PhD in the Henry A. Rowland department of Physics and Astronomy in 2007.

Beginning in the fall of 2013 Michael will work at the Center for Integrated Nanotechnology, a Department of Energy funded user-facility associated with Sandia National Lab.